ELSEVIER

J. Non-Newtonian Fluid Mech. 120 (2004) 189–205

Journal of Non-Newtonian Fluid Mechanics

www.elsevier.com/locate/jnnfm

Rheology of polymer blends with matrix-phase viscoelasticity and a narrow droplet size distribution

Marco Dressler [a,*], Brian J. Edwards [b]

[a] *Laboratory of Food Process Engineering, Institute of Food Science and Nutrition, ETH-Zürich, Zürich CH-8092, Switzerland*
[b] *Department of Chemical Engineering, The University of Tennessee, Knoxville, TN 37996, USA*

Received 6 October 2003; received in revised form 5 February 2004

This article is part of a Special Volume containing papers from the 3rd International Workshop on Nonequilibrium Thermodynamics and Complex Fluids

Abstract

A Hamiltonian framework of non-equilibrium thermodynamics is adopted to construct a set of dynamical continuum equations for a polymer blend with matrix viscoelasticity and a narrow droplet size distribution that is assumed to obey a Weibull distribution function. The microstructure of the matrix is described in terms of a conformation tensor. The variable droplet distribution is described in terms of two thermodynamic variables: the droplet shape tensor and the number density of representative droplets. A Hamiltonian functional in terms of the thermodynamic variables is introduced and a set of time evolution equations for the system variables is derived. Sample calculations for homogenous flows and constant droplet distribution are compared with data of a PIB/PDMS blend and a HPC/PDMS blend with high viscoelastic contrast. For the PIB/PDMS blend, satisfactory predictions of the flow curves are obtained. Sample calculations for a blend with variable droplet distribution are performed and the effect of flow on the rheology, droplet morphology, and on the droplet distribution are discussed. It is found that deformation can increase or decrease the dispersity of the droplet morphology for the flows investigated herein.

Keywords: Non-equilibrium thermodynamics; Polymer blends; Constant-volume models; Rheological characterization; Oblate/prolate drops; Non-uniform droplet distribution

1. Introduction

The purpose of this paper at the 3rd International Workshop on Non-Equilibrium Thermodynamics is to present recent developments in our ongoing study of the rheology and morphology of polymer blends. In a recent article [1], we examined the effects of matrix-phase viscoelasticity on the rheology and morphology of Newtonian droplets subjected to both shear and elongational flow fields. This previous article demonstrated that matrix-phase viscoelasticity was very important for quantifying the deformation-induced shape changes in the dispersed phase droplets, as well as the overall rheological responses of the blends.

In this paper, we extend the model introduced in the previous article [1] to incorporate phenomena of break-up and coalescence of droplets in a crude way. This is done through the introduction of a Weibull distribution function to quantify the size of the droplets. As in the prior article, we are not so much striving for quantitative accuracy in model prediction, but are instead attempting to develop an understanding for what type of effects are necessary in order to render an accurate physical understanding of polymer blend rheology. Here we add to this understanding by examining the extent to which droplet break-up and coalescence affect the rheology and morphological characteristics of typical polymer blends. At the end, we should be able to draw some relevant conclusions about the importance of the size distribution of droplets on these important materials.

The present article is organized as follows. In the next section, we give a description of the system we want to model. We introduce the relevant thermodynamic variables and we make a constitutive assumption for the system Hamiltonian. In Section 3, a set of time evolution equations for the thermodynamic variables is derived in a Hamiltonian framework of non-equilibrium thermodynamics. In Section 4, we present sample calculations for start-up and steady-state shear and uniaxial elongational flow. We compare model calculations with experimental data of real polymer blends, and we in-

* Corresponding author. Tel.:+41 1 632 5349; fax:+41 1 632 1155.
E-mail address: dressler@ilw.agrl.ethz.ch (M. Dressler).

0377-0257/$ – see front matter © 2004 Elsevier B.V. All rights reserved.
doi:10.1016/j.jnnfm.2004.02.009

vestigate the effect of flow on the droplet distribution. In the final section, we summarize our results.

2. The thermodynamic system

In the present work, the polymer blend is considered as a continuum with internal microstructure consisting of two immiscible phases. The thermodynamic variables in a continuum description of matter are statistical mechanical averages over all constituent molecules and other microstructural components of the continuum. The macroscopic flow of the blend is quantified in terms of the momentum density field, $\boldsymbol{M}$, defined as the velocity of a fluid particle, $\boldsymbol{v}$, times its density, ρ. The average orientation and deformation of the matrix molecules at a fixed position in space is described in terms of the contravariant, second-rank conformation tensor field, $\boldsymbol{C}$. For a polymer blend with a narrow, non-uniform droplet size distribution, the Weibull distribution function [2],

$$f(R) = \frac{1}{V}\gamma q R^{q-1}\,\mathrm{e}^{-\gamma R^q}, \tag{1}$$

is assumed to give a reasonable description of the average droplet size distribution, where $R > 0$ is a dimensionless droplet radius, $f(R)$ is the number density of micro-droplets with radii between R and $R + \mathrm{d}R$ per unit volume, V, and $q > 1$, $\gamma > 0$ are positive real numbers. The above droplet distribution function (DDF) is fully specified if the location, $\tilde{R}$, and the height, $f(\tilde{R})$, of its absolute maximum are known. Therefore, we introduce two representative thermodynamic variables to account for the non-uniform droplet morphology of the polymer blend. The droplet shape tensor, $\boldsymbol{S}$, is related to the location of the maximum of the DDF, $\mathrm{tr}\boldsymbol{S}/3 \equiv \tilde{R}$, and is a contravariant, second-rank tensor field, with the constraint $\det\boldsymbol{S} = 1$ to account for volume preservation of the micro-droplets. A scalar variable, n, which represents the average number density of micro-droplets of representative shape $\boldsymbol{S}$, is related to the height of the maximum of the DDF, $n \equiv f(\tilde{R})$. We emphasize that the two internal variables, $\boldsymbol{S}$ and n, are representative microstructural variables of the polymer blend. The full droplet morphology is described in terms of an appropriate DDF, here $f(R)$. Hence our set of thermodynamical variables is $x \equiv [\boldsymbol{M}, \boldsymbol{C}, \boldsymbol{S}, n]$.

The droplet shape tensor, $\boldsymbol{S}$, has a direct connection to the droplet morphology since the eigenvalues of $\boldsymbol{S}$ are the squared semiaxes of the ellipsoidal droplets and the determinant is their volume [3]. Therefore, we chose the droplet shape tensor to describe the droplet morphology instead of an anisotropy tensor of the Doi-Ohta type [4,5]. Very recently, Almusallam et al. [6] considered the anisotropy tensor approach in the framework of the Tomotika Theory to describe droplet break-up and coalescence in polymer blends.

With the thermodynamic variables introduced above, we make now a constitutive assumption for the Hamiltonian functional, which represents the total energy of the polymer blend. Here, we study a system that is envisioned as a superposition of a Maxwell fluid with characteristic elastic constant, K, an elastic droplet interface with interfacial tension, Γ', and a non-linear coupling of matrix and interfacial elasticity with the variable number density, n, of representative micro-droplets, $\boldsymbol{S}$:

$$\begin{aligned} H_{\mathrm{m}}[\boldsymbol{M}, \boldsymbol{C}, \boldsymbol{S}, n] &= K[\boldsymbol{M}] + A[\boldsymbol{C}, \boldsymbol{S}, n] \\ &= \int \Bigg[\frac{M_\alpha M_\alpha}{2\rho} + \frac{1}{2}(1-\phi)G\frac{K}{k_{\mathrm{B}}T} I_1^{\mathrm{C}} - \frac{1}{2}(1-\phi)G \\ &\times \ln(\det\frac{K\boldsymbol{C}}{k_{\mathrm{B}}T}) + \frac{1}{2}\phi\Gamma\frac{n}{n_0} I_2^{\mathrm{S}} - \frac{1}{6}\phi\Gamma\frac{K}{k_{\mathrm{B}}T} \\ &\times \ln(\frac{n}{n_0}) I_1^{\mathrm{C}} \epsilon(I_1^{\mathrm{S}}, I_2^{\mathrm{S}}) \Bigg]\, \mathrm{d}^3x. \end{aligned} \tag{2}$$

In this expression, I_n^{C} and I_n^{S} denote the n-th invariant of $\boldsymbol{C}$ and $\boldsymbol{S}$, respectively, $\phi = 1/V\int_0^\infty f(R)\mathrm{d}R$ is the constant total volume fraction of droplets, G is the elastic modulus of the matrix, $\Gamma = \Gamma'/R_0$ where R_0 is a representative droplet radius in the undeformed state, n_0 denotes the representative number density of micro-droplets at equilibrium, and $\epsilon = \epsilon(I_1^{\mathrm{S}}, I_2^{\mathrm{S}})$ is a measure for the asphericity of the droplets. Eq. (2) represents the kinetic energy of the system (first term in the integral) plus a linear superposition of the Helmholtz free energy of a system of Hookean springs (second and third terms) and the energy of the elastic interface, with I_2^{S} being associated with the surface area (fourth term). Note that the energy of the elastic interface is proportional to the relative representative number of micro-droplets, n/n_0, and therefore increases linearly with n. To represent the dynamic effects that determine the representative number density of droplets away from equilibrium, a fifth term is added to the Hamiltonian. We consider here a logarithmic term in n/n_0 similar to the Flory/Huggins mixing term. This mixing term is taken to depend on both microstructural variables, $\boldsymbol{C}$ and $\boldsymbol{S}$. The mixing term depends on the microstructural tensor $\boldsymbol{C}$, since the conformation of the matrix molecules influences droplet shape and hence the break-up and coalescence processes. Here, we have chosen a linear dependence of the mixing term on the trace of the conformation tensor, I_1^{C}, for simplicity. Furthermore, the mixing term depends on the average asphericity of the micro-droplets, which can be expressed in terms of the non-unit scalar invariants of the droplet shape tensor, $\epsilon = \epsilon(I_1^{\mathrm{S}}, I_2^{\mathrm{S}})$. Here we take the first invariant of the droplet configuration tensor, $\epsilon = I_1^{\mathrm{S}}$, to express the asphericity of the droplet. Consequently, we have $\epsilon = 3$ at equilibrium and $\epsilon \to \infty$ as the micro-droplets are stretched into long fibres or compressed into thin sheets. More elaborate expressions for the asphericity parameter in terms of the first and the second invariants of the droplet shape tensor can be introduced if necessary.

The subscript "m" in the Hamiltonian denotes that the description of the polymer blend is purely mechanical; i.e., we will not consider the transfer of mechanical energy into internal degrees of freedom. Instead, we study an isothermal and incompressible system. Note that Eq. (2) duly sat-

isfies the consistency requirement that, at equilibrium in absence of any stress and when the droplet shape is spherical, $\boldsymbol{S}_{\text{equil}} = \boldsymbol{\delta}$, the Hamiltonian is minimized for $n = n_0$, which can be considered in general as a function of the viscosity ratio and the temperature.

In the next section, a set of dynamical time evolution equations for the variables $x = [\boldsymbol{M}, \boldsymbol{C}, \boldsymbol{S}, n]$ will be constructed in order to describe the dynamical behavior of the polymer blend. To do this, we adopt an appropriate framework of non-equilibrium thermodynamics.

3. Derivation of continuum-level evolution equations

In this section, we wish to present the main steps in the construction of the macroscopic flow equations for the set of variables $x = [\boldsymbol{M}, \boldsymbol{C}, \boldsymbol{S}, n]$. A detailed presentation of the thermodynamic modeling of complex materials in terms of internal variables is explained in Ref. [7]. In the Hamiltonian framework of non-equilibrium thermodynamics, the dynamical evolution equations for the polymer blend are derived from the master equation

$$\frac{\mathrm{d}F}{\mathrm{d}t} = \{F, H_{\mathrm{m}}\} + [F, H_{\mathrm{m}}], \tag{3}$$

where $F = F[x]$ is an arbitrary functional of a set of field variables x, H_{m} denotes the Hamiltonian or the generator of the dynamics, $\{\cdot,\cdot\}$ and $[\cdot,\cdot]$ denote the Poisson and dissipation brackets, respectively, and $\mathrm{d}\cdot/\mathrm{d}t$ is the time derivative.

The physical variables, x, for the description of the blend are the momentum density, $\boldsymbol{M} = \rho\boldsymbol{v}$, an unconstrained contravariant second-rank tensor, $\boldsymbol{C}$, describing the microstructure of the continuous phase (i.e., the conformation of the polymer molecules in the matrix), a constrained contravariant second-rank tensor, $\boldsymbol{S}$, describing a representative ellipsoidal droplet shape of the DDF, and the representative number density of micro-droplets with shape tensor $\boldsymbol{S}$, n: hence $x = [\boldsymbol{M}, \boldsymbol{C}, \boldsymbol{S}, n]$. Since the dispersed phase is assumed to be incompressible, we impose the microstructural constraint, $\det\boldsymbol{S} = 1$, to account for volume preservation of the deforming ellipsoidal microdroplets.

For single droplets with diameters larger than microns (40–500 μm), the approximation of ellipsoidal droplet shape has been investigated experimentally by Guido and Villone [8] and by Hu and Lips [9] in simple shear flow and in planar hyperbolic flow, respectively. Implicitly, we assume the validity of the ellipsoidal droplet and constant-volume assumptions on smaller length scales than those examined experimentally.

To obtain a set of continuum equations using Eq. (3), one has to derive the Poisson bracket and to postulate a dissipation bracket, as well as the generator of the dynamics, Eq. (2). The Poisson bracket needs to be expressed in terms of $\boldsymbol{M}$, $\boldsymbol{C}$, $\boldsymbol{S}$ and n, and is given as

$$\begin{aligned}
\{F, H_{\mathrm{m}}\} = &-\int\left[\frac{\delta F}{\delta M_\gamma}\nabla_\beta\left(\frac{\delta H_{\mathrm{m}}}{\delta M_\beta}M_\gamma\right) - \frac{\delta H_{\mathrm{m}}}{\delta M_\gamma}\nabla_\beta\left(\frac{\delta F}{\delta M_\beta}M_\gamma\right)\right]\mathrm{d}^3x - \int\left[\frac{\delta F}{\delta C_{\alpha\beta}}\nabla_\gamma\left(\frac{\delta H_{\mathrm{m}}}{\delta M_\gamma}C_{\alpha\beta}\right) - \frac{\delta H_{\mathrm{m}}}{\delta C_{\alpha\beta}}\nabla_\gamma\left(\frac{\delta F}{\delta M_\gamma}C_{\alpha\beta}\right)\right]\\
&\times\mathrm{d}^3x - \int C_{\gamma\alpha}\left[\frac{\delta H_{\mathrm{m}}}{\delta C_{\alpha\beta}}\nabla_\gamma\left(\frac{\delta F}{\delta M_\beta}\right) - \frac{\delta F}{\delta C_{\alpha\beta}}\nabla_\gamma\left(\frac{\delta H_{\mathrm{m}}}{\delta M_\beta}\right)\right]\mathrm{d}^3x - \int C_{\gamma\beta}\left[\frac{\delta H_{\mathrm{m}}}{\delta C_{\alpha\beta}}\nabla_\gamma\left(\frac{\delta F}{\delta M_\alpha}\right) - \frac{\delta F}{\delta C_{\alpha\beta}}\nabla_\gamma\left(\frac{\delta H_{\mathrm{m}}}{\delta M_\alpha}\right)\right]\\
&\times\mathrm{d}^3x - \int\left[\frac{\delta F}{\delta S_{\alpha\beta}}\frac{\delta H_{\mathrm{m}}}{\delta M_\gamma}\nabla_\gamma\left(S_{\alpha\beta}\right) - \frac{\delta H_{\mathrm{m}}}{\delta S_{\alpha\beta}}\frac{\delta F}{\delta M_\gamma}\nabla_\gamma\left(S_{\alpha\beta}\right)\right]\mathrm{d}^3x - \int S_{\gamma\alpha}\left[\frac{\delta H_{\mathrm{m}}}{\delta S_{\alpha\beta}}\nabla_\gamma\left(\frac{\delta F}{\delta M_\beta}\right) - \frac{\delta F}{\delta S_{\alpha\beta}}\nabla_\gamma\left(\frac{\delta H_{\mathrm{m}}}{\delta M_\beta}\right)\right]\\
&\times\mathrm{d}^3x - \int S_{\gamma\beta}\left[\frac{\delta H_{\mathrm{m}}}{\delta S_{\alpha\beta}}\nabla_\gamma\left(\frac{\delta F}{\delta M_\alpha}\right) - \frac{\delta F}{\delta S_{\alpha\beta}}\nabla_\gamma\left(\frac{\delta H_{\mathrm{m}}}{\delta M_\alpha}\right)\right]\mathrm{d}^3x + \frac{2}{3}\int S_{\alpha\beta}\left[\frac{\delta H_{\mathrm{m}}}{\delta S_{\alpha\beta}}\nabla_\gamma\left(\frac{\delta F}{\delta M_\gamma}\right) - \frac{\delta F}{\delta S_{\alpha\beta}}\nabla_\gamma\left(\frac{\delta H_{\mathrm{m}}}{\delta M_\gamma}\right)\right]\\
&\times\mathrm{d}^3x - \int\left[\frac{\delta F}{\delta n}\nabla_\beta\left(\frac{\delta H_{\mathrm{m}}}{\delta M_\beta}n\right) - \frac{\delta H_{\mathrm{m}}}{\delta n}\nabla_\beta\left(\frac{\delta F}{\delta M_\beta}n\right)\right]\mathrm{d}^3x.
\end{aligned} \tag{4}$$

This bracket shares the properties of a Poisson bracket since it is bilinear, it is antisymmetric, and it satisfies the Jacobi identity. The first integral represents the Poisson bracket for the structureless, incompressible, and isothermal fluid. The second, third, and fourth integrals represent the Poisson bracket for a contravariant, unconstrained, second-rank tensorial variable, $\boldsymbol{C}$. The last integral is the Poisson bracket for the scalar variable, n. These brackets were derived following standard reduction procedures from Hamilton's principle of least action in Refs. [10–14,7]. The remaining four integrals represent the Poisson bracket for a constrained, contravariant, second-rank tensorial variable, $\boldsymbol{S}$, with $\det\boldsymbol{S} = 1$, and it was derived in Ref. [15] by adopting a suitable mapping transformation.

For the dissipation bracket, we introduce the expression

$$\begin{aligned}
[F, H_{\mathrm{m}}] = &-\int \Lambda^{\mathrm{C}}_{\alpha\beta\gamma\epsilon}\frac{\delta F}{\delta C_{\alpha\beta}}\frac{\delta H_{\mathrm{m}}}{\delta C_{\gamma\epsilon}}\mathrm{d}^3x - \int \Lambda^{\mathrm{S}}_{\alpha\beta\gamma\epsilon}\frac{\delta F}{\delta S_{\alpha\beta}}\frac{\delta H_{\mathrm{m}}}{\delta S_{\gamma\epsilon}}\mathrm{d}^3x \quad + \frac{1}{3}\int \Lambda^{\mathrm{S}}_{\alpha\beta\gamma\epsilon}S_{\rho\eta}S^{-1}_{\alpha\beta}\frac{\delta F}{\delta S_{\rho\eta}}\frac{\delta H_{\mathrm{m}}}{\delta S_{\gamma\epsilon}}\mathrm{d}^3x - \int \Lambda^{n}\frac{\delta F}{\delta n}\frac{\delta H_{\mathrm{m}}}{\delta n}\mathrm{d}^3x\\
&- \int A_{\alpha\beta\gamma\epsilon}\left(\frac{\delta F}{\delta C_{\alpha\beta}}\frac{\delta H_{\mathrm{m}}}{\delta S_{\gamma\epsilon}} + \frac{\delta H_{\mathrm{m}}}{\delta C_{\alpha\beta}}\frac{\delta F}{\delta S_{\gamma\epsilon}}\right)\mathrm{d}^3x + \frac{1}{3}\int A_{\alpha\beta\gamma\epsilon}\left(\frac{\delta F}{\delta C_{\alpha\beta}}\frac{\delta H_{\mathrm{m}}}{\delta S_{\rho\eta}}S_{\rho\eta}S^{-1}_{\gamma\epsilon} + \frac{\delta H_{\mathrm{m}}}{\delta C_{\alpha\beta}}\frac{\delta F}{\delta S_{\rho\eta}}S_{\rho\eta}S^{-1}_{\gamma\epsilon}\right)\mathrm{d}^3x,
\end{aligned} \tag{5}$$

with the four phenomenological matrices $\boldsymbol{\Lambda}^{\mathrm{C}}$, $\boldsymbol{\Lambda}^{\mathrm{S}}$, Λ^n, and $\boldsymbol{A}$. The above dissipation bracket represents a generaliza-

tion of the dissipation bracket for the Two Coupled Maxwell Modes Model in Refs. [7,16] to a system that is described in terms of an unconstrained conformation tensor, $\boldsymbol{C}$, a constrained representative droplet tensor, $\boldsymbol{S}$, with $\det\boldsymbol{S} = 1$, and a variable representative number density of micro-droplets, n.

The first integral in the above dissipation bracket is the relaxation of the viscoelastic matrix. The second and the third integrals account for the relaxation of the droplet inclusions under the auspices of the constraint $\det\boldsymbol{S} = 1$, and they were derived in Ref. [15]. The fourth integral with the phenomenological matrix Λ^n is the relaxation of the representative number density of micro-droplets in the fluid. The last two integrals, involving the phenomenological matrix $\boldsymbol{A}$, describe the coupling of the viscoelastic matrix fluid with the droplet interface. They were derived with the procedure developed in Ref. [15]. In the above dissipation bracket, we neglect viscous dissipation of the matrix fluid since it appears implicitly in the Maxwell viscosity, $G\lambda_C$, and droplet diffusivity. The latter phenomenon can be included into the dissipation bracket to obtain more sophisticated dynamic equations for the system if so desired.

An irreversible coupling of the number density of droplets with the droplet shape tensor, $\boldsymbol{S}$, is not considered in Eq. (5) because it gives an antisymmetric contribution to the dissipation bracket, which does not contribute to the rate of mechanical energy dissipation. We wish to consider only contributions to the dissipation bracket that yield a non-vanishing rate of mechanical energy dissipation. (This is a completely arbitrary consideration, but we believe that it is better for a preliminary work to keep the final set of evolution equations as simple as possible.) The rate of mechanical energy dissipation associated with the above dissipation bracket, Eq. (5), will be discussed below.

The Poisson and dissipation brackets yield the following general set of dynamical evolution equations:

$$\rho\frac{\partial v_\alpha}{\partial t} = -\rho v_\beta\nabla_\beta v_\alpha - \nabla_\alpha p + \nabla_\beta\sigma_{\alpha\beta}, \tag{6a}$$

$$\frac{\partial C_{\alpha\beta}}{\partial t} = -v_\gamma\nabla_\gamma C_{\alpha\beta} + C_{\alpha\gamma}\nabla_\gamma v_\beta + C_{\beta\gamma}\nabla_\gamma v_\alpha - \Lambda^{\mathrm{C}}_{\alpha\beta\gamma\epsilon}\frac{\delta H_\mathrm{m}}{\delta C_{\gamma\epsilon}} - A_{\alpha\beta\gamma\epsilon}\frac{\delta H_\mathrm{m}}{\delta S_{\gamma\epsilon}} + \frac{1}{3}A_{\alpha\beta\gamma\epsilon}\frac{\delta H_\mathrm{m}}{\delta S_{\rho\nu}}S_{\rho\nu}S^{-1}_{\gamma\epsilon}, \tag{6b}$$

$$\frac{\partial S_{\alpha\beta}}{\partial t} = -v_\gamma\nabla_\gamma S_{\alpha\beta} - \frac{2}{3}\nabla_\gamma v_\gamma S_{\alpha\beta} + S_{\alpha\gamma}\nabla_\gamma v_\beta + S_{\beta\gamma}\nabla_\gamma v_\alpha - \Lambda^{\mathrm{S}}_{\alpha\beta\gamma\epsilon}\frac{\delta H_\mathrm{m}}{\delta S_{\gamma\epsilon}} + \frac{1}{3}\Lambda^{\mathrm{S}}_{\rho\eta\gamma\epsilon}S_{\alpha\beta}S^{-1}_{\rho\eta}\frac{\delta H_\mathrm{m}}{\delta S_{\gamma\epsilon}} - A_{\alpha\beta\gamma\epsilon}\frac{\delta H_\mathrm{m}}{\delta C_{\gamma\epsilon}} + \frac{1}{3}A_{\rho\nu\gamma\epsilon}\frac{\delta H_\mathrm{m}}{\delta C_{\rho\nu}}S^{-1}_{\gamma\epsilon}S_{\alpha\beta}, \tag{6c}$$

$$\frac{\partial n}{\partial t} = -\nabla_\alpha(nv_\alpha) - \Lambda^n\frac{\delta H_\mathrm{m}}{\delta n}. \tag{6d}$$

Eq. (6a) is the momentum balance equation in a spatial description of macroscopic fluid flow, where the pressure and the extra stress tensor have been denoted with p, $\boldsymbol{\sigma}$, respectively. Pressure and velocity are thus viewed as averaged quantities at each location in space-time coordinates; i.e., they are coarse-grained averages of the matrix fluid particles and droplets contained in the fluid particle at coordinates $(\boldsymbol{x}, t)$. They arise naturally through the mathematical structure of the Poisson bracket. The pressure obeys a Poisson equation with appropriate boundary conditions, and the extra stress tensor is obtained as

$$\sigma_{\alpha\beta} = 2C_{\alpha\gamma}\frac{\delta H_\mathrm{m}}{\delta C_{\gamma\beta}} + 2S_{\alpha\gamma}\frac{\delta H_\mathrm{m}}{\delta S_{\gamma\beta}} - \frac{2}{3}S_{\gamma\epsilon}\frac{\delta H_\mathrm{m}}{\delta S_{\gamma\epsilon}}\delta_{\alpha\beta}. \tag{7}$$

Eq. (6b) is the conformation tensor equation describing the average deformation and orientation of polymer molecules in the matrix. The first three terms on the righthand-side of Eq. (6b) represent the upper-convected derivative of an unconstrained, second-rank contravariant tensorial variable, and they arise from the mathematical structure of the Poisson bracket, Eq. (4). The remaining three terms on the righthand-side of Eq. (6b) are of dissipative nature. The third term captures the relaxational dynamics of the matrix molecules and the last two terms in Eq. (6b) account for a possible influence of droplet deformation on the conformation tensor dynamics. Eq. (6c) is the droplet shape tensor equation describing the average shape and orientation of representative micro-droplets in the blend. The first four terms on the righthand-side of Eq. (6c) represent a generalized upper-convected derivative for a second-rank, contravariant tensorial variable with the constraint $\det\boldsymbol{S} = 1$, obtained from the Poisson bracket. The last four terms in Eq. (6c) arise from the dissipation bracket, and account for the relaxation of micro-droplets (fifth and sixth terms) and the influence of the conformation tensor dynamics on the droplet dynamics (the last two terms). With the procedure developed by Edwards et al. [15], it can be shown for Eq. (6c) that $\det\boldsymbol{S}$ is a conserved quantity independent of the mathematical form of the phenomenological matrices $\boldsymbol{\Lambda}^{\mathrm{C}}$, $\boldsymbol{\Lambda}^{\mathrm{S}}$, $\boldsymbol{A}$, and the Hamiltonian, $H_\mathrm{m}[\boldsymbol{M}, \boldsymbol{C}, \boldsymbol{S}, n]$.

In order to obtain a specific set of time evolution equations that is generated by an appropriate system Hamiltonian (e.g., Eq. (2)), we have to specify expressions for the phenomenological matrices $\boldsymbol{\Lambda}^{\mathrm{C}}$, $\boldsymbol{\Lambda}^{\mathrm{S}}$, Λ^n, and $\boldsymbol{A}$ introduced in the dissipation bracket, Eq. (5), and appearing in the above set of general system equations, Eqs. (6a)–(6d). This is done in the following paragraphs.

To describe the relaxation of the matrix fluid, we adopt the phenomenological matrix of the extended White–Metzner (EWM) Model of Souvaliotis and Beris [17] (see, e.g., Ref. [7]). This is

$$\Lambda^{\mathrm{C}}_{\alpha\beta\gamma\epsilon} = \frac{1}{2\lambda_\mathrm{C}G}\frac{k_\mathrm{B}T}{K}(\mathrm{tr}\tilde{\boldsymbol{C}}/3)^{-k}(C_{\alpha\gamma}\delta_{\beta\epsilon} + C_{\alpha\epsilon}\delta_{\beta\gamma} + C_{\beta\gamma}\delta_{\alpha\epsilon} + C_{\beta\epsilon}\delta_{\alpha\gamma}), \tag{8}$$

where λ_C is a characteristic relaxation time associated with the continuous phase and we have introduced the elastic modulus of the continuous phase G. In the above relaxation

matrix, the effective relaxation time of the matrix phase, $\lambda(\tilde{\boldsymbol{C}}) \equiv \lambda_C(\mathrm{tr}\tilde{\boldsymbol{C}})^k$, is allowed to depend on the first invariant of the scaled conformation tensor, $\tilde{\boldsymbol{C}} = \boldsymbol{C}K/(k_BT)$, and on the EWM power-law index, k. For $k = 0$, we recover the relaxation matrix of the Maxwell Model. In conjunction with the $\boldsymbol{C}$-terms in the Hamiltonian, Eq. (2), and with $\boldsymbol{A} = 0$ and $k = 0$, this expression gives the Upper-Convected Maxwell Model (UCMM) for the matrix phase.

We adopt the following anisotropic expression for the relaxation matrix of the interface:

$$\Lambda^S_{\alpha\beta\gamma\epsilon} = \frac{1}{\lambda_S \Gamma}\left[\frac{(1+p)^2 p}{2}\left(S_{\alpha\gamma}\delta_{\beta\epsilon} + S_{\alpha\epsilon}\delta_{\beta\gamma} + S_{\beta\gamma}\delta_{\alpha\epsilon} + S_{\beta\epsilon}\delta_{\alpha\gamma}\right) + \frac{3p}{I_1^S I_2^S}\left(\delta_{\alpha\gamma}\delta_{\beta\epsilon} + \delta_{\alpha\epsilon}\delta_{\beta\gamma}\right)\right], \tag{9}$$

where λ_S is a characteristic time scale associated with the elastic interface and I_1^S, I_2^S are the first and the second invariants of $\boldsymbol{S}$, respectively [1]. The first term in the square brackets accounts for droplets that deform into oblates for start-up of steady shearing flow, the second term accounts for droplets that deform into prolates for start-up of steady shearing flow. The difference between oblate and prolate droplet shapes is illustrated in subsequent figures, which will be explained in more detail in the next section. The quantity p is a phenomenological parameter that controls whether the droplet deformation is more oblate or prolate, and it depends on the viscous and/or elastic properties of the two phases.

In what follows, we wish to consider two different possibilities to relate the phenomenological coefficient, p, to the material properties of the polymer blend, since the physical mechanisms that govern droplet deformation in non-Newtonian liquids are not well known and the issue is a topic of ongoing research, see e.g., Refs. [18–20]. If droplet deformation into oblate or prolate configurations is assumed to depend on the viscous properties of the two phases, then p should be taken as the negative viscosity ratio of the blend components, i.e., $p = -\eta_d/\eta_c$. (The fact that p has to be a negative quantity will be discussed below, when we examine the rate of mechanical energy dissipation due to droplet relaxation, $\boldsymbol{\Lambda}^S$—see also Ref. [1].) If droplet deformation into oblate or prolate configurations is assumed to depend on the viscoelastic properties of the interface, instead of the Newtonian viscosity of the droplet phase, one may introduce an interfacial viscosity, $\eta^* = \Gamma\lambda_S$, and define $p = -\eta^*/\eta_c$. Then, if $\eta_c = G\lambda_c$ is identified as a Maxwellian viscosity of the continuous phase, p becomes a dependent quantity that combines the viscoelastic properties of the matrix and the interface, $p = -\Gamma\lambda_S/G\lambda_C$. Otherwise, one may introduce an additional viscous dissipation matrix into the bracket, Eq. (5), to take into account explicitly the Newtonian flow behavior of the matrix. For the sample calculations in the subsequent paragraphs, we investigate the model equations for $p = -\eta_d/\eta_c$ as well as $p = -\eta^*/\eta_c$.

For the phenomenological matrix Λ^n, the following general expression is introduced:

$$\Lambda^n = 2f_c\frac{n_0 n}{\lambda_n \Gamma}, \tag{10}$$

where λ_n is a characteristic time scale of the break-up/coalescence process and f_c is a general function of the phenomenological parameter, p, and the scalar invariants of the conformation tensor and the droplet shape tensor, $f_c = f_c(p, \tilde{\boldsymbol{C}}, \boldsymbol{S})$. This quantity can be related to the probability of the coalescence process [21]. In the sample calculations, we will take $f_c = 1$ for simplicity; i.e., we neglect a direct influence of the viscosity ratio on the break-up/coalescence processes in the framework of the present study.

The phenomenological matrix $\boldsymbol{A}$ is adopted in analogy to the coupling matrix introduced in Ref. [16,7,1]:

$$A_{\alpha\beta\gamma\epsilon} = \frac{1}{2}\frac{(1+p)^2\theta}{\sqrt{G\Gamma\lambda_C\lambda_S}}(\mathrm{tr}\tilde{\boldsymbol{C}}/3)^{-k/2}(C_{\alpha\gamma}S_{\beta\epsilon} + C_{\alpha\epsilon}S_{\beta\gamma} + C_{\beta\gamma}S_{\alpha\epsilon} + C_{\beta\epsilon}S_{\alpha\gamma}), \tag{11}$$

where θ is a phenomenological coupling parameter. For $\theta > 0$ this phenomenological matrix gives oblate droplet configurations. Note that the coupling matrix is defined to vanish for $p = -1$. The phenomenological coefficient, θ, may be taken as a function of the scalar invariants of the structural variables, if so desired; however, here we want to work with θ being a constant real number, for simplicity.

We mention that the prefactors that contain the viscosity ratio in the phenomenological matrices, Eqs. (8), (9) and (11), have been introduced ad hoc: $\zeta_o = (1+p)^2 p$, $\zeta_p = p$, $\zeta_c = (1+p)^2$. It may be necessary to adopt more appropriate functional dependencies if one wants to fit experimental data or to make predictions over an extended range or viscosity ratios, p.

In order to rationalize the thermodynamic admissibility of the phenomenological matrices of Eqs. (8)–(11), we consider the rate of mechanical energy dissipation generated by the Hamiltonian, (2):

$$\frac{dH_m}{dt} = [H_m, H_m] \leq 0. \tag{12}$$

This is a decreasing function of time [7]. Eq. (12) is obtained from Eq. (3) by exploiting the antisymmetry of the Poisson bracket and the fact that mechanical energy has to be dissipated into internal degrees of freedom in the long time limit. Inequality (12) is the appropriate condition to give a physically meaningful description of the system, and it can lead to counterintuitive results for the range of thermodynamically admissible phenomenological coefficients adopted herein; e.g., a negative viscosity ratio appearing in Eq. (9) [1]. Mathematical criteria that are imposed directly onto the dissipative phenomenological coefficients, e.g., on the relaxation times, λ_C and λ_S, on the coupling parameter, θ, or on the

dissipative coefficient, p, do not necessarily satisfy Inequality (12) and may therefore lead to aphysical results. This will become evident in the following paragraph, where we evaluate Eq. (12) for the dissipation bracket of Eq. (5).

For the dissipation bracket of Eq. (5), Inequality (12) is equivalent to

$$
\begin{aligned}
[H_\mathrm{m}, H_\mathrm{m}] = [H_\mathrm{m}, H_\mathrm{m}]_\mathrm{C} + [H_\mathrm{m}, H_\mathrm{m}]_\mathrm{S} + [H_\mathrm{m}, H_\mathrm{m}]_n + [H_\mathrm{m}, H_\mathrm{m}]_\mathrm{CS} = -\frac{1}{2\lambda_\mathrm{C}} \int (\mathrm{tr}\tilde{\boldsymbol{C}}/3)^{-k} \Bigg[(1-\phi)^2 G \\
\times \left(\frac{K}{k_\mathrm{B}T} I_1^\mathrm{C} + \frac{k_\mathrm{B}T}{K} I_{-1}^\mathrm{C} - 6 \right) + 2\phi(1-\phi)\Gamma \ln\left(\frac{n}{n_0}\right) I_1^\mathrm{S} \left(1 - \frac{K}{3k_\mathrm{B}T} I_1^\mathrm{C} \right) + \frac{1}{9}\phi^2 \frac{\Gamma^2}{G} \left(\ln\frac{n}{n_0} \right)^2 \\
\times \frac{K}{k_\mathrm{B}T} I_1^\mathrm{C} I_1^\mathrm{S} I_1^\mathrm{S} \Bigg] \mathrm{d}^3x - \frac{(1+p)^2 p \phi^2 \Gamma}{2\lambda_\mathrm{S}} \int \left[\left(\frac{n}{n_0}\right)^2 \left(3 - \frac{1}{3} I_1^\mathrm{S} I_2^\mathrm{S} \right) + \frac{1}{3} \frac{K}{k_\mathrm{B}T} \frac{n}{n_0} \ln\left(\frac{n}{n_0}\right) I_1^\mathrm{C} I_2^\mathrm{S} \left(\frac{I_1^\mathrm{S} I_1^\mathrm{S}}{3 I_2^\mathrm{S}} - 1 \right) \right] \\
\times \mathrm{d}^3x - \frac{p\phi^2\Gamma}{\lambda_\mathrm{S}} \int \left[\frac{n}{n_0} - \frac{K}{3k_\mathrm{B}T} \ln\left(\frac{n}{n_0}\right) \frac{I_1^\mathrm{C}}{I_1^\mathrm{S}} \right] \left[\frac{n}{n_0} I_2^\mathrm{S} \left(3 \frac{I_1^\mathrm{S}}{(I_2^\mathrm{S})^2} - 1 \right) + \frac{1}{2} \ln\left(\frac{n}{n_0}\right) \frac{K}{k_\mathrm{B}T} \frac{I_1^\mathrm{C}}{I_2^\mathrm{S}} \left(I_1^\mathrm{S} I_2^\mathrm{S} - 9 \right) \right] \\
\times \mathrm{d}^3x - \frac{\phi^2\Gamma}{2\lambda_n} \int f_\mathrm{c} \left(\frac{n}{n_0} I_2^\mathrm{S} I_2^\mathrm{S} - \frac{2}{3} \frac{K}{k_\mathrm{B}T} I_1^\mathrm{C} I_1^\mathrm{S} I_2^\mathrm{S} + \frac{1}{9} \left(\frac{K}{k_\mathrm{B}T} \right)^2 (I_1^\mathrm{C} I_1^\mathrm{S})^2 \frac{n}{n_0} \right) \mathrm{d}^3x - \frac{(1+p)^2 \phi\theta}{\sqrt{\lambda_\mathrm{C}\lambda_\mathrm{S}}} \sqrt{\frac{\Gamma}{G}} \frac{K}{k_\mathrm{B}T} \\
\times \int (\mathrm{tr}\tilde{\boldsymbol{C}}/3)^{-k/2} \left[(1-\phi) G - \frac{1}{3}\phi\Gamma \ln\left(\frac{n}{n_0}\right) I_1^\mathrm{S} \right] \left[\frac{n}{n_0} \left(I_1^\mathrm{S} C_{\alpha\beta} S_{\alpha\beta} - C_{\alpha\gamma} S_{\beta\gamma} S_{\alpha\beta} - \frac{2}{3} I_1^\mathrm{C} I_2^\mathrm{S} \right) \right. \\
\left. - \frac{1}{3} \frac{K}{k_\mathrm{B}T} \ln\left(\frac{n}{n_0}\right) I_1^\mathrm{C} \left(C_{\alpha\beta} S_{\alpha\beta} - \frac{1}{3} I_1^\mathrm{C} I_1^\mathrm{S} \right) \right] \mathrm{d}^3x \le 0, \qquad (13)
\end{aligned}
$$

where $I_{-1}^\mathrm{C} = C_{\alpha\alpha}^{-1} = I_2^\mathrm{C}/I_3^\mathrm{C}$. The first integral is the mechanical energy dissipation of a Maxwell fluid, $[H_\mathrm{m}, H_\mathrm{m}]_\mathrm{C}$, the second and third integrals are the mechanical energy dissipation due to droplet relaxation including oblate and prolate relaxation, $[H_\mathrm{m}, H_\mathrm{m}]_\mathrm{S}$, the fourth integral is the rate of mechanical energy dissipation due to the change of the representative droplet number density, $[H_\mathrm{m}, H_\mathrm{m}]_n$, and the fifth integral is the rate of mechanical energy dissipation due to the irreversible coupling of the matrix fluid and the droplet interface, $[H_\mathrm{m}, H_\mathrm{m}]_\mathrm{CS}$. The above expression for the rate of mechanical energy dissipation is negative, if each of the five integrals are negative.

In the following, we want to evaluate generically the first three integrals in In Inequality (13) for start-up of a homogeneous, weak flow; i.e., we consider a vanishing coupling parameter, $\theta = 0$, and the limit of infinite break-up time, λ_n, to find the correct range of thermodynamically admissible phenomenological coefficients p. Note that all terms proportional to $\ln(n/n_0)$ in the first three integrals vanish in the limit $\theta = 0$, $\lambda_n \to \infty$. Numerical calculations corroborate that the scalar invariants of the structural variables increase upon start-up of steady flow (except the third invariant of the droplet shape tensor, $\det \boldsymbol{S} = 1$). The invariant I_{-1}^C assumes values above its equilibrium value, $I_{-1}^\mathrm{C} = 3K/(k_\mathrm{B}T)$; however, the variations in I_{-1}^C are small compared to the variations of I_1^C. Therefore, the first integral in In Inequality (13), which corresponds to the mechanical dissipation rate of the UCMM, anyway, is negative since the expression in parentheses is positive (since the relaxation times, λ_C, λ_S, and the elastic moduli, G, Γ, are positive numbers). Due to $I_1^\mathrm{S} \ge 3$ and $I_2^\mathrm{S} \ge 3$ for non-vanishing flow, the expressions in parentheses in the second and the third integrals are negative. Consequently, the phenomenological friction coefficient, p, has to be negative, $p < 0$, to give a negative dissipation rate due to droplet relaxation. For small values of the coupling parameter, $|\theta| \ll 1$, this quantity has to be positive to yield a negative dissipation of mechanical energy due to the coupling between the two microstructural variables. Our analysis shows that the constraint $\det(\boldsymbol{S}) = 1$ and the functional form of the thermodynamic potential, $E_\mathrm{S} = \Gamma\phi I_2^\mathrm{S}/2$, produce this counterintuitive example of a phenomenological dissipative coefficient being negative. Note that the aspect of a negative friction coefficient in the droplet configuration equation is not worked out rigorously by Grmela et al. [22] and Yu et al. [23]. With the general set of dynamical time evolution equations, (6a)–(6d), and the constitutive assumptions for the dissipative matrices, Eqs. (8)–(11), we can now write down the set of dynamical equations generated by the Hamiltonian, Eq. (2).

Evaluating the Volterra derivatives of the Hamiltonian (2) and inserting the phenomenological matrices of Eqs. (8)–(11) into Eqs. (6a)–(6d), we obtain the following time evolution equations for the structural variables and the representative droplet number density:

$$
\begin{aligned}
\frac{\partial C_{\alpha\beta}}{\partial t} = &-v_\gamma \nabla_\gamma C_{\alpha\beta} + C_{\alpha\gamma}\nabla_\gamma v_\beta + C_{\beta\gamma}\nabla_\gamma v_\alpha \\
&- \frac{1-\phi}{\lambda_\mathrm{C}} (\mathrm{tr}\tilde{\boldsymbol{C}}/3)^{-k} C_{\alpha\beta} + (1-\phi)\frac{k_\mathrm{B}T}{\lambda_\mathrm{C}K} (\mathrm{tr}\tilde{\boldsymbol{C}}/3)^{-k} \delta_{\alpha\beta} \\
&+ \frac{\phi\Gamma}{3\lambda_\mathrm{C}G} (\mathrm{tr}\tilde{\boldsymbol{C}}/3)^{-k} \ln\left(\frac{n}{n_0}\right) I_1^\mathrm{S} C_{\alpha\beta} \\
&- \frac{1}{2}\sqrt{\frac{\Gamma}{G}} \frac{(1+p)^2\phi\theta}{\sqrt{\lambda_\mathrm{C}\lambda_\mathrm{S}}} (\mathrm{tr}\tilde{\boldsymbol{C}}/3)^{-k/2} \left\{ \frac{n}{n_0} \right.
\end{aligned}
$$

$$\times\left[(I_1^S\delta_{\gamma\epsilon}-S_{\gamma\epsilon})(C_{\alpha\gamma}S_{\beta\epsilon}+C_{\beta\gamma}S_{\alpha\epsilon})-\frac{4}{3}I_2^S C_{\alpha\beta}\right]$$
$$-\frac{K}{3k_BT}\ln\left(\frac{n}{n_0}\right)I_1^C$$
$$\times\left(C_{\alpha\gamma}S_{\beta\gamma}+C_{\beta\gamma}S_{\alpha\gamma}-\frac{2}{3}I_1^S C_{\alpha\beta}\right)\Bigg\}, \tag{14a}$$

$$\frac{\partial S_{\alpha\beta}}{\partial t}=-v_\gamma\nabla_\gamma S_{\alpha\beta}-\frac{2}{3}\nabla_\gamma v_\gamma S_{\alpha\beta}+S_{\alpha\gamma}\nabla_\gamma v_\beta+S_{\beta\gamma}\nabla_\gamma v_\alpha$$
$$-\frac{(1+p)^2 p\phi}{\lambda_S}\frac{n}{n_0}\left(\frac{1}{3}I_1^S S_{\alpha\beta}-S_{\alpha\gamma}S_{\gamma\beta}\right)$$
$$+\frac{p\phi}{\lambda_S}\left[\frac{n}{n_0}-\frac{K}{3k_BT}\ln\left(\frac{n}{n_0}\right)\frac{I_1^C}{I_1^S}\right]\left(S_{\alpha\beta}-\frac{3\delta_{\alpha\beta}}{I_2^S}\right)$$
$$-\frac{K}{2k_BT}\frac{(1+p)^2\theta}{\sqrt{\lambda_C\lambda_S}}(\mathrm{tr}\tilde{\boldsymbol{C}}/3)^{-k/2}$$
$$\times\left[(1-\phi)\sqrt{\frac{G}{\Gamma}}-\frac{\phi}{3}\sqrt{\frac{\Gamma}{G}}\ln\left(\frac{n}{n_0}\right)I_1^S\right]$$
$$\times\left(C_{\alpha\gamma}S_{\beta\gamma}+C_{\beta\gamma}S_{\alpha\gamma}-\frac{2}{3}I_1^C S_{\alpha\beta}\right), \tag{14b}$$

$$\frac{\partial n}{\partial t}=-\nabla_\alpha(nv_\alpha)-\frac{\phi f_c I_2^S}{\lambda_n}n+\frac{\phi f_c K I_1^C I_1^S}{3k_BT\lambda_n}n_0. \tag{14c}$$

Eq. (14a) is the conformation tensor equation. For $\theta=0$, $k=0$, and $n=n_0$, we recover the UCMM. For $\theta\neq 0$ and $p\neq -1$, we have a non-trivial coupling of the droplet phase to the matrix phase. This means that the droplet deformation induces changes in the average conformation of the molecules in the matrix phase. Eq. (14b) is the droplet shape tensor equation describing the dynamics of a representative drop of the droplet distribution. The first four terms on the righthand-side of Eq. (14b) are the reversible contributions to the droplet dynamics, the fifth term in Eq. (14b) accounts for oblate droplets, and the sixth term accounts for prolate droplets. The last term captures two additional influences on the droplet dynamics: (i) the local polymer conformation in the matrix phase and (ii) the variable representative number density of droplets. Eq. (14c) is the number density time evolution equation with a reversible and two irreversible contributions. The second term on the righthand-side of Eq. (14c) has a negative sign and it accounts for a decrease of the representative number density of micro-droplets, i.e., droplet coalescence. This term is proportional to the number density of droplets, n, cf. Ref. [21]. The last term on the righthand-side of Eq. (14c) has a positive sign, and it accounts for an increase of the representative number density of droplets, i.e., break-up. Note that we have a single time scale for break-up and coalescence, λ_n. Furthermore, note that an equilibrium of coalescence and break-up rates is predicted by Eq. (14c) at any steady state. The last two terms on the righthand-side of Eq. (14c) represent effective coalescence and break-up rates, which involve the dispersed phase concentration and the invariants of the two structural variables. Though the time scale for coalescence and break-up are identical, the time evolution equations give different rates of coalescence and break-up far from thermodynamic equilibrium.

The elastic extra stress tensor of the blend is the linear combination of the extra stress tensor of the two components. With Eq. (2), the general expression of Eq. (7) for the extra stress tensor is equivalent to

$$\sigma_{\alpha\beta}=\sigma_{\alpha\beta}^C+\sigma_{\alpha\beta}^S=(1-\phi)G\frac{K}{k_BT}C_{\alpha\beta}-(1-\phi)G\delta_{\alpha\beta}$$
$$+\phi\Gamma\frac{n}{n_0}\left(I_1^S S_{\alpha\beta}-S_{\alpha\gamma}S_{\gamma\beta}-\frac{2}{3}I_2^S\delta_{\alpha\beta}\right)-\frac{\phi\Gamma K}{3k_BT}$$
$$\times\ln\left(\frac{n}{n_0}\right)\left[I_1^C S_{\alpha\beta}+I_1^S C_{\alpha\beta}-\frac{1}{3}I_1^C I_1^S\delta_{\alpha\beta}\right]. \tag{15}$$

For the dilute regime ($\phi\to 0$), we have mainly a stress contribution due to the matrix phase and the droplet configuration is governed by the coupling term in Eq. (14b). For the concentrated regime ($\phi\to 1$), the extra stress is due to the droplet phase and the non-linear coupling terms are the only contributions in the conformation tensor evolution equation, Eq. (14a).

4. Sample calculations

The set of continuum equations, Eq. (6a), (14a)–(14c), derived in the previous section, has been solved for various combinations of physical parameter values to determine its characteristic features for various homogeneous flows, characterized by the velocity gradient tensor, $\nabla\boldsymbol{v}$. These equations have been rendered dimensionless using quantities $\tilde{t}=t/\sqrt[3]{\lambda_C\lambda_S\lambda_n}$, $\tilde{\boldsymbol{C}}=K/k_BT\boldsymbol{C}$, $\tilde{\boldsymbol{S}}=\boldsymbol{S}$, $\tilde{n}=n/n_0$, and $\tilde{\boldsymbol{\sigma}}=\boldsymbol{\sigma}/(\sqrt{G\Gamma})$. In all that follows, we omit the tilde over dimensionless quantities. Note that there is a one-to-one relationship between the parameters, q, γ, in the Weibull distribution function and the thermodynamic variables, $\boldsymbol{S}$, n. The parameter q is obtained by solving the non-linear equation $n=f(\tilde{R})$, where $\tilde{R}\equiv 1/3\mathrm{tr}\boldsymbol{S}$ is the location of the maximum of the DDF and n, $\boldsymbol{S}$ are the solutions of the continuum equations for a given velocity field. Then also the second parameter of the Weibull distribution function is fixed since $\tilde{R}^q=(q-1)/\gamma q$.

4.1. PIB/PDMS blend with low viscoelastic contrast

In this subsection, we show solutions of the continuum equations for a constant DDF and for data of a polyisobutene (PIB, $\eta_d=86\,\mathrm{Pa\,s}$)/polydimethylsiloxane (PDMS, $\eta_c=195\,\mathrm{Pa\,s}$, $\Psi_{1c}=10.4\mathrm{Pa\,s}^2$) blend [24]. Interfacial tension between the blend components is $\Gamma'=0.0023\mathrm{N/m}$ [24]. With the UCMM and the relationship for the interfacial elastic modulus, we estimate $G\approx 7300\,\mathrm{Pa}$ and $\Gamma=230\,\mathrm{Pa}$ for an average droplet radius of $10\,\mu\mathrm{m}$.

Fig. 1 shows calculations for the pure matrix fluid with $G = 7300$Pa and $\phi = 0$ (solid lines) and two PIB/PDMS blends with $G/\Gamma = 30$, $\phi = 0.1$ (dashed lines) and $G/\Gamma = 30$, $\phi = 0.3$ (dotted lines). The EWM power-law index has been taken as $k = -2$ to recover the shear thinning behavior for the matrix fluid and the phenomenological coupling coefficient has been chosen as $\theta = 0.01$. The phenomenological parameter, p, is not taken as the viscosity ratio of the blend components, but it is related to the interfacial elasticity in Figs. 1 and 2, $p = -\eta^*/\eta_C$. The ratio of relaxation times λ_C/λ_S is adjusted to fit experimental data.

Fig. 1a–d show the steady-state viscometric functions of the PIB/PDMS blend, which are normalized with respect to their steady-state values. Fig. 1a shows the steady flow curves of $\eta_S(\dot\gamma)$ for the pure PDMS matrix fluid (solid line) and for the PIB/PDMS blends with $\phi = 0.1$ (dashed line) and $\phi = 0.3$ (dotted line). Experimental data points were taken from Ref. [24]. We obtain a satisfactory fit for the flow curve of the matrix fluid (circles) and for the $\phi = 0.1$ blend (squares). For volume fractions as high as $\phi = 0.3$, the power-law behavior is not recovered with our set of parameters. Since the model is strictly applicable only to low concentration blends, this observation is to be expected.

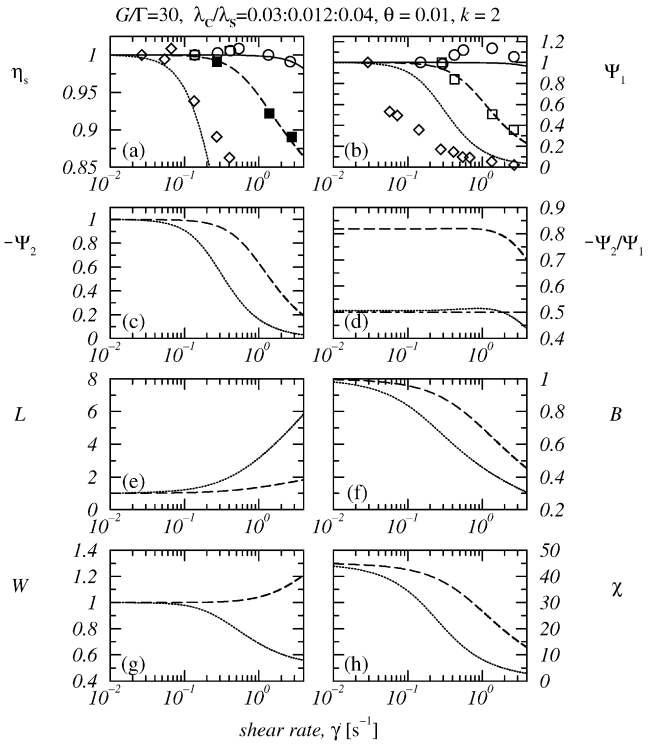

Fig. 1. Model predictions of the continuum equations for constant droplet distribution $n = 1$, as a function of shear-rate for three different dispersed phase concentrations, $\phi = 0$ (solid lines), 0.1 (dashed lines), and 0.3 (dotted lines). Other model parameters are $G = 7300$, $k = -2$ (for $\phi = 0$); $G/\Gamma = 30$, $\theta = 0.01$, $k = -2$ (for $\phi \neq 0$); $p = -\Gamma\lambda_S/G\lambda_C$. The ratio of relaxation times has been taken as a fitting parameter: $\lambda_C/\lambda_S = 0.03$ ($\phi = 0$), 0.012 ($\phi = 0.1$), 0.04 ($\phi = 0.3$). The viscometric functions have been normalized with respect to their zero shear-rate values. Symbols are experimental data from Ref. [24].

Fig. 1b displays the steady-state first normal stress coefficient as a function of shear-rate. Also here we observe a satisfactory fit for the $\phi = 0.1$ blend, whereas the onset of the shear thinning behavior is not recovered for the $\phi = 0.3$ blend. Fig. 1c–h show further solutions of the system equations for which no experimental data are available. Note that for the pure matrix fluid, the EWM model predicts $\Psi_2 = 0$ and no droplet morphology is present. Therefore, only the predictions of the two blends are reported in the remaining graphs of Fig. 1. Fig. 1c displays the shear thinning behavior of the second normal stress coefficient, Ψ_2, for the $\phi = 0.1$ and the 0.3 blend. Fig. 1d shows the ratio of the two normal stress coefficients. For $\phi = 0.1$, we recover $\Psi_2/\Psi_1 \approx -0.8$ being considerably larger than for polymer melts, whereas for $\phi = 0.3$ a smaller value of $\Psi_2/\Psi_1 \approx -0.5$ is recovered from the system equations. This value is close to the stress tensor predictions of the Maffettone-Minale (MM) Model, $\Psi_2/\Psi_1 = -0.5$, cf. Ref. [23], which has also been included in Fig. 1d. In Fig. 1e–h we display the morphological characteristics of the polymer blend, which are represented by the average magnitude of the three semiaxes of the ellipsoidal droplets and the average orientation of the droplets with respect to the flow direction. The semiaxes of the droplets are the square roots of the eigenvalues of the droplet configuration tensor, $\boldsymbol{S}$ [3]. The droplet semiaxes in the flow direction, in the direction of the shear gradient, and in the direction

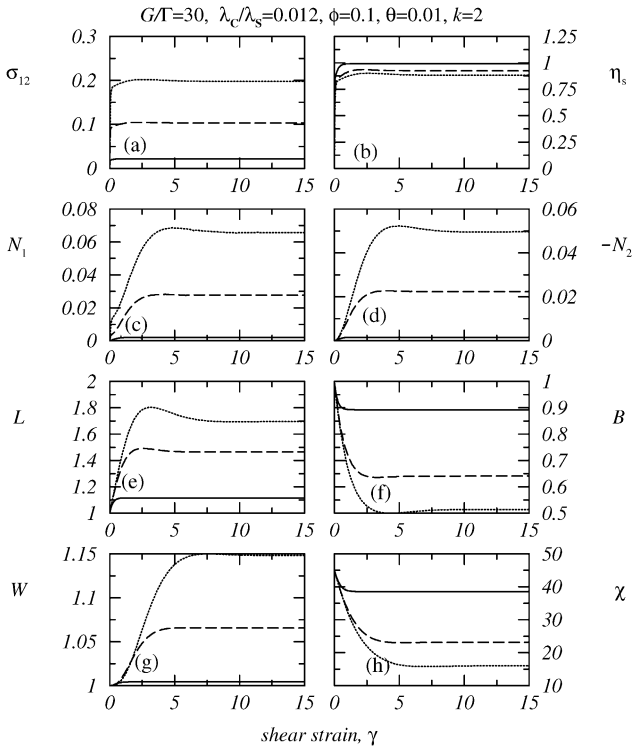

Fig. 2. The same as Fig. 1 for start-up of steady shearing flow as a function of shear strain for the $\phi = 0.1$ blend and three different shear rates, $\dot\gamma = 0.27\,s^{-1}$ (solid lines), $1.38\,s^{-1}$ (dashed lines), and $2.77\,s^{-1}$ (dotted lines) corresponding to the filled symbols in Fig. 1. The shear viscosities in (b) are normalized with respect to the zero shear-rate viscosity.

of the vorticity axis are denoted with L, B, W, respectively. For steady shear flow, the major droplet axis, L, increases and the minor droplet axis, B, decreases with respect to the equilibrium droplet radius (Fig. 1e and f). However, the vorticity axis, W, can be greater than, smaller than, or equal to unity upon start-up of flow and the droplets are thus either oblate or prolate. In Fig. 1g, we have oblate droplets ($W > 1$) for the $\phi = 0.1$ blend and prolate droplets ($W < 1$) for the $\phi = 0.3$ blend. The orientation angle, χ, is the angle between the eigenvector corresponding to the largest eigenvalue of the $\boldsymbol{S}$-tensor and the flow direction; it is defined as $\chi = 1/2 \arctan[2S_{12}/(S_{11} - S_{22})]$. This quantity decreases for increasing shear rate, Fig. 1h.

Very recently, Guido et al. [19] studied the steady-state deformation of single Newtonian droplets in a viscoelastic matrix. For the continuous and the dispersed phase a non-Newtonian polyisobutylene (PIB) and silicon oil were used, respectively. For viscosity ratios $p = -1$ and -0.1, steady-state prolate droplets have been observed.

Fig. 2 displays transient solutions of the continuum equations for start-up of steady shearing flow for the $\phi = 0.1$ blend assuming again a constant DDF. Sample calculations were carried out for three different shear rates, $\dot{\gamma} = 0.27\,\mathrm{s}^{-1}$ (solid lines), $1.38\,\mathrm{s}^{-1}$ (dashed lines), and $2.77\,\mathrm{s}^{-1}$ (dotted lines), which correspond to the abscissas of the filled squares in Fig. 1a. Material parameters are the same as in Fig. 1 for the 10wt% PIB/PDMS blend, i.e., $G/\Gamma = 30$, $\theta = 0.01$, $k = -2$, and $\lambda_C/\lambda_S = 0.012$. Fig. 2a–d display the transient viscometric behavior of the system equations showing a typical non-linear viscoelastic response as encountered often in synthetic polymer rheology. The transient shear stress, σ_{12}, and the shear viscosity, $\eta_s = \sigma_{12}/\dot{\gamma}$, (Fig. 2a and b) show a rapid approach to their steady-state values, which are attained at $\gamma \approx 5$ shear strain units. The shear viscosity in Fig. 2b has been normalized with respect to the zero shear-rate value. The first normal stress difference in Fig. 2c is positive and shows a monotonic increase for the lowest shear-rate ($\dot{\gamma} = 0.27\,\mathrm{s}^{-1}$, solid line), whereas a slight overshoot is seen for the higher shear rates ($\dot{\gamma} = 1.38\,\mathrm{s}^{-1}$, $2.77\,\mathrm{s}^{-1}$, broken lines). The steady-state value of N_1 is attained at strains of $\gamma \approx 10$, being twice as high as the strains that are necessary to attain a steady-state shear stress. The first normal stress difference is approximately one order of magnitude smaller than the shear stress. The second normal stress difference in Fig. 2d is negative, and of the same order of magnitude as the first normal stress difference. Both normal stress differences, N_1 and N_2, show a similar qualitative behavior as a function of strain rate in the regime of shear rates shown in Fig. 2.

Fig. 2e–h display the transient morphological properties of the $\phi = 0.1$ blend for start-up of steady shearing flow. For the low shear-rate, $\dot{\gamma} = 0.27\,\mathrm{s}^{-1}$ (solid line), we recover a monotonic approach of the droplet axes and the orientation angle towards their steady-state values. For the highest shear-rate, $\dot{\gamma} = 2.77\,\mathrm{s}^{-1}$ (dotted line), a pronounced overshoot is observed in L, which goes along with slight undershoots in the two minor droplet axes, B and W. For all shear rates shown in Fig. 2, the droplet shape evolves towards a oblate, sheet-like configuration.

Levitt et al. [25] report transient morphological measurements of a single polypropylene droplet in a viscoelastic matrix with $G/G_d \approx 0.3$, where G_d is the elastic modulus of the dispersed phase. Immediately after start-up of steady shear flow, an increase of the vorticity axis to 40% of its equilibrium value is observed. For higher shear strains, the vorticity axis decreases and a prolate droplet is recovered.

In the above sample calculations, we see that the transient first normal stress difference is approximately one order of magnitude smaller than the shear stress ($\sigma_{12} \gg N_1$) for the shear rate regime investigated in Fig. 2. The changes that the externally imposed flow field induces in the droplet morphology are as large as 70% for the major droplet axis, L. For the minor droplet axis, B, and for the vorticity axis, W, we recover variations of 50 and 15%, respectively, for a shear-rate as high as $\dot{\gamma} = 2.77\,\mathrm{s}^{-1}$, and a steady state is recovered from the model. This may be due to the viscoelastic similarity between the matrix and the interface, which is quantified in terms of $G/\Gamma = 30$ and $\lambda_C/\lambda_S = 0.012$. With these values, we calculate $\Psi_{1c}/\Psi_{1d} \approx 4 \times 10^{-3}$ for the ratio of zero shear-rate first normal stress coefficients.

In what follows, we wish to solve the continuum equations for a polymer blend with a high viscoelastic contrast between the matrix phase and the interface and to investigate whether a large viscoelastic contrast of the blend components allows for highly deformed microstructural constituents such as fibres or sheets. This is of technological importance since in processing one is interested in the creation of a strongly deformed droplet morphology with a high amount of interface.

4.2. HPC/PDMS600 blend with high viscoelastic contrast

In Figs. 3 and 4, we present sample calculations for a polymer blend with a strong viscoelastic contrast between the two phases. Also for the present calculations, we assume a constant DDF, i.e., $n = 1$. However, we take the phenomenological coefficient, p, as an independent quantity, i.e., $p = -\eta_d/\eta_c$ corresponds to the viscosity ratio of the blend components. Polymer blends with a strong viscoelastic contrast are of technological importance because it is possible to produce highly deformed inclusions (e.g., fibres or sheets), by means of modest mechanical deformation of the blend. Kernick and Wagner [26], e.g., examined a polymer blend of 5 wt.% hydroxypropyl cellulose (HPC, $\eta_d \approx 300\,\mathrm{Pa\,s}$) in a PDMS ($\eta_d = 600\mathrm{Pa\,s}$) matrix by means of rheology and small angle neutron scattering. In this system, the large viscoelastic contrast between the matrix and the dispersed liquid-crystalline polymer phase is due to the phenomenon that HPC displays a phase transiton from the tumbling to the flow aligning regime that correlates with a sign change of the first normal stress difference causing a $\Psi_{1c}/\Psi_{1d} \gg 1$.

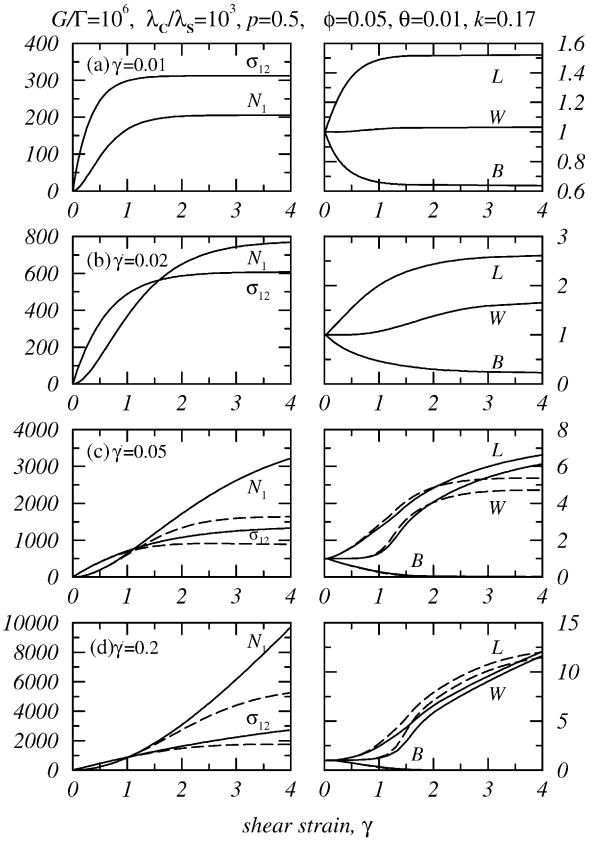

Fig. 3. The transient shear stress, σ_{12}, and first normal stress difference, N_1 (left column) and the transient droplet axes, L, B, W (right column) for four different shear rates $\dot{\gamma} = 0.01$ (first row), 0.02 (second row), 0.05 (third row), and 0.2 (fourth row). The blend components have a strong viscoelastic contrast with $G/\Gamma = 10^6$ and $\lambda_C/\lambda_S = 10^3$. The phenomenological coefficient $p = -0.5$ is taken as the viscosity ratio of the blend components, i.e., an independent model parameter. Other model parameters are $\phi = 0.05$, $\theta = 0.01$, and $k = -0.17$. The dashed lines in (c) and (d) are for $k = -1.3$.

Fig. 3 shows calculations for a polymer blend with dispersed phase concentration $\phi = 0.05$, and viscosity ratio $p = -0.5$. In the present model, the droplet phase is assumed to be Newtonian and hence anelastic. Only the first normal stress difference of the matrix and the interface can be varied in the model to tune the viscoelastic difference between the two phases. In order to mimic the strong viscoelastic contrast between the two phases, we have taken $G/\Gamma = 10^6$, and $\lambda_C/\lambda_S = 10^3$; i.e., the ratio of the zero shear-rate first normal stress coefficient of the matrix and the interface in the steady state is $\Psi_{1c}/\Psi_{1d} = 10^{12}$. The EWM power-law index for the continuous phase has been chosen as $k = -0.13$, reproducing the shear thinning behavior of the PDMS matrix (cf. Fig. 7 in Ref. [26]).

Fig. 3 shows transient rheological and morphological properties of the model blend for start-up of steady shearing flow for four different shear rates: $\dot{\gamma} = 0.01$ (a), $\dot{\gamma} = 0.02$ (b), $\dot{\gamma} = 0.05$ (c), and $\dot{\gamma} = 0.2$ (d). For the lowest shear-rate portrayed in Fig. 3a, we observe a monotonic increase of

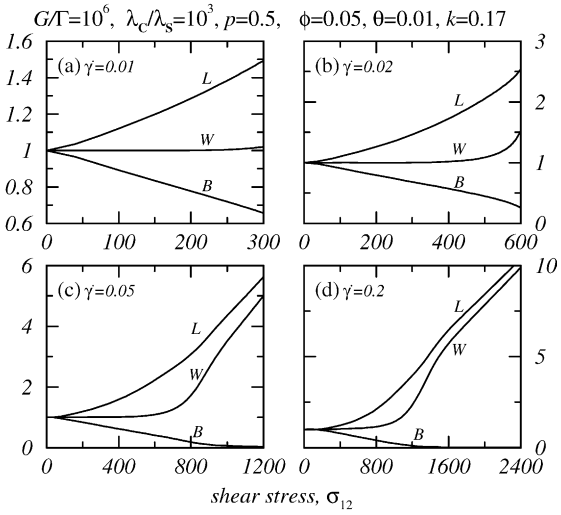

Fig. 4. The same as Fig. 3 for the transient droplet semiaxes, L, B, and W, as functions of the transient shear stress, σ_{12}, for four different shear rates: (a) $\dot{\gamma} = 0.01$, (b) $\dot{\gamma} = 0.02$, (c) $\dot{\gamma} = 0.05$, (d) $\dot{\gamma} = 0.2$.

the shear stress, σ_{12}, and the first normal stress difference, N_1, to their respective steady-state values. Note that in the low shear-rate regime, the shear stress is always bigger than the first normal stress difference, which corresponds to a system with a small viscoelastic contrast as studied, e.g., in Figs. 1 and 2. In this shear-rate regime, only relatively small droplet deformations are observed. In particular, the vorticity axis of the doplet increases slightly and reaches a steady-state value that is approximately 4% above its equilibrium value in the undeformed state. In Fig. 3b ($\dot{\gamma} = 0.02$), the shear stress is bigger than the first normal stress difference only in the small shear strain regime, $\gamma < 1.5$ (γ^* denotes the shear strain where $\sigma_{12} = N_1$ which we can identify from Fig. 3b–d). For $\gamma > \gamma^*$, the first normal stress difference becomes greater than the shear stress which may be due to the high values of G/Γ and λ_C/λ_S. The crossover of the two stresses correlates with a strong increase of the vorticity axis of the droplet, W, for shear strains $\gamma \approx \gamma^*$. At the steady state, the vorticity axis, W, is approximately 18% above its equilibrium value, whereas for $\dot{\gamma} = 0.01$ an increase of approximately 4% is observed at the steady state (Fig. 3a). For even higher shear rates, $\dot{\gamma} = 0.05$ and 0.2, the crossover of the first normal stress difference, N_1, and the shear stress, σ_{12}, shifts towards smaller shear strains ($\gamma^* \approx 1$), and the first normal stress difference becomes considerably larger than the shear stress (Fig. 3c and d). For these shear rates, two different droplet deformation regimes can be identified. For $\gamma > \gamma^*$, we observe only a slight droplet widening in the vorticity direction, whereas the droplet widening becomes very strong for $\gamma \gtrsim \gamma^*$. In the latter strain-rate regime, the strong droplet widening correlates with the droplet extension in the flow direction and the droplets deform into thin disks with $L \approx W \approx 10$ and $B \approx 0$. For smaller EWM power-law indices, the steady state is recovered at smaller shear strains. This is illustrated

in Fig. 3c and d, where predictions for $k = -1.3$ (dashed lines) are included.

Fig. 4 shows the transient droplet semiaxes as functions of the transient shear stress for four different shear rates. We observe that the time evolution behavior of the droplet semiaxes correlates with the shear stress. For the two highest shear rates in Fig. 4c–d, the major droplet axis, L, and the vorticity axis, W, start to increase linearly for $\sigma_{12} \gtrsim 800$ and $\gtrsim$1200, approximately.

In the following subsection, we want to present sample calculations for the full set of continuum equations that have been derived in the previous section, taking into account a variable DDF, which is allowed to interact mutually with the externally imposed flow field, the viscoelasticity of the matrix phase, and the droplet deformation as dictated by the model equations.

4.3. Blends with variable and constant droplet distribution

In what follows, we present sample calculations for a blend with a variable DDF, and we compare our model predictions with the predictions of a reduced model that assumes a constant DDF, i.e., $n = 1$. We do so in order to investigate the effect of a non-uniform DDF on the morphological properties and the rheological response of the deforming blend. Again, the phenomenological coefficient, p, is taken as an independent model parameter for the present set of sample calculations; i.e., $p = -\eta_d/\eta_c$ corresponds to the viscosity ratio of the blend components. Moreover, we take $k = 0$ for the EWM power-law index; i.e., we neglect the shear thinning behavior of the matrix fluid for the sample calculations in this section.

Grizzuti and Bifulco [27] studied the effect of coalescence and break-up on the steady-state morphology of immiscible polymer blends in shear flow. In their experimental studies, coalescence and break-up phenomena prevail over the effects of droplet deformation.

Fig. 5 shows the rheometric and the morphological properties as a function of shear-rate, $\dot{\gamma}$, for two model blends with $p = -0.25$, $G/\Gamma = 4$ (solid lines) and $p = -1.25$, $G/\Gamma = 4$ (dashed lines), solving the full set of model equations (6a) and (14a)–(14c) for steady shearing flow. The dispersed phase concentration is $\phi = 0.1$. The thin dotted lines in Fig. 5 are predictions for a constant droplet distribution and analogous material parameters. We have taken $\lambda_C\lambda_S/\lambda_n^2 = 1$ for the ratio of relaxation times of the blend, and a phenomenological coupling coefficient $\theta = 0.001$.

Fig. 5a–d show the non-linear rheometric properties as predicted from the system equations for steady shear flow. All viscometric functions possess a Newtonian plateau for low shear rates, a power-law regime for intermediate shear rates, and another Newtonian plateau in the high shear-rate regime (Fig. 5a–c). The ratio of the normal stress coefficients in Fig. 5d is non-trivial and decreases with increasing shear-rate. The viscometric properties of the blends with

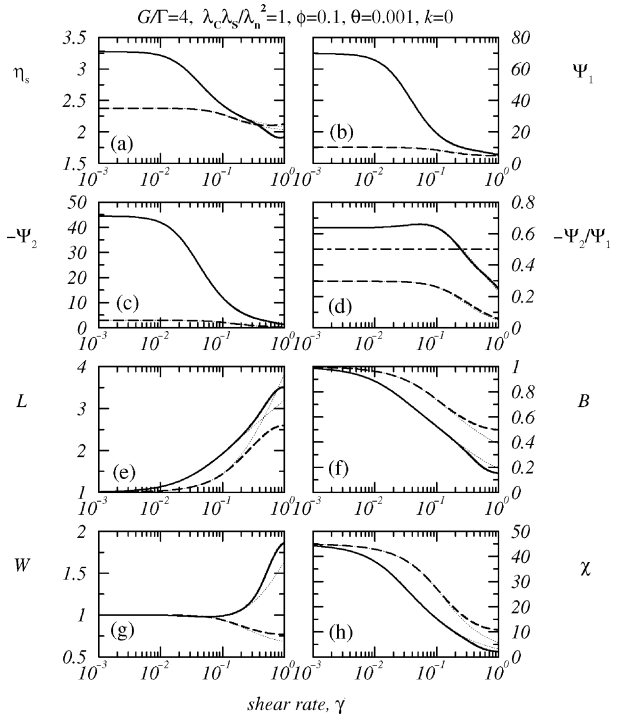

Fig. 5. Model predictions of the continuum equations for a variable DDF as functions of shear-rate for two different viscosity ratios, $p = -0.25$ (solid lines) and $p = -1.25$ (dashed lines). For the ratio of elastic moduli, the relaxation times, the coupling parameter, and the EWM power-law index, we chose $G/\Gamma = 4$, $\lambda_C\lambda_S/\lambda_n^2 = 1$, $\theta = 0.001$, and $k = 0$, respectively. Dispersed phase concentration is $\phi = 0.1$. The thin dotted lines are model preditions for a constant droplet distribution, i.e., $n = 1$.

variable and constant DDF are very similar for the present choice of model parameters.

Fig. 5e–h show the deformation induced microstructural changes of the droplet morphology and the orientation of the micro-droplets with respect to the external flow field. The major droplet axis, L, increases and the minor droplet axis, B, decreases with increasing shear-rate. For the low viscosity ratio blend, $p = -0.25$, we observe stronger variations in the major and in the minor droplet axes than for the $p = -1.25$ blend. The steady-state behavior of the vorticity axis of the droplet, W, is different for the two blends. Whereas a droplet widening effect, $W > 1$, is calculated for the low viscosity ratio, $p = -0.25$, a droplet compression effect, $W < 1$, is obtained for the high viscosity ratio, $p = -1.25$. The orientation angle, χ, decreases as a function of shear-rate. From Fig. 5e–h we see that a variable DDF influences the steady-state morphological properties as obtained from the model equations, if we compare with the prediction for a constant DDF. This is especially true in the high shear-rate regime, $\dot{\gamma} \gtrsim 0.2$. Note that for very high shear rates, the viscometric and the morphological properties of the blend seem to approach constant plateau values. Finally, it should be mentioned that the continuum equations predict steady-state solutions for a wide shear-rate regime, extending from a low shear-rate region with a lower Newtonian

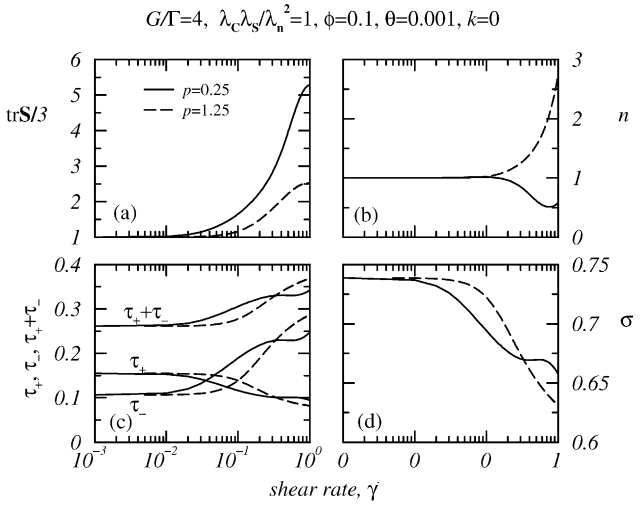

Fig. 6. The same as Fig. 5 for the properties of the steady DDF, $f(\mathrm{tr}\boldsymbol{S}/3)$: (a) position of the maximum, $\mathrm{tr}\boldsymbol{S}/3$, (b) maximum of the distribution function, n, (c) volume fraction of residual droplets left and right from the inflection points $R_\pm$ (τ_+, τ_-) and total volume fraction of residual droplets ($\tau_+ + \tau_-$), (d) volume fraction of the droplets around the maximum of the droplet distribution function, σ.

plateau to high shear rates with an upper Newtonian plateau.

In Fig. 6, we examine the properties of the steady-state DDF for $p = -0.25$ (solid lines) and $p = -1.25$ (dashed lines) as functions of shear-rate. We use the same model parameters as in Fig. 5. Fig. 6a shows the average radius of the representative micro-droplets. This quantity increases for both viscosity ratios reported in Fig. 6 as the shear-rate, $\dot\gamma$, is increased. For shear rates as high as $\dot\gamma \approx 0.8$, the increase in the average droplet radius becomes less pronounced and seems to reach a plateau value (cf. Fig. 5). The behavior of the average droplet radius shown in Fig. 6a corresponds to a shift of the location of the maximum of the DDF towards higher values of $\tilde R \equiv \mathrm{tr}\boldsymbol{S}/3$ as the shear rate, $\dot\gamma$, is increased (cf. Fig. 7).

Fig. 6b shows the solution of the droplet number density equation, Eq. (14c), for steady shear flow. We note that the representative number density of micro-droplets decreases for the $p = -0.25$ blend, whereas it increases for the $p = -1.25$ blend with increasing shear-rate, $\dot\gamma$. This means that the steady-shear DDF is smeared out for $p = -0.25$ (cf. Fig. 7a), and it is compressed for $p = -1.25$ (cf. Fig. 7b). Hence our model equations predict a shear-induced droplet coalescence in the low viscosity regime, and a shear-induced droplet break-up in the higher viscosity ratio regime.

In Fig. 6c and d, we show several characteristic droplet volume fractions, τ_-, τ_+, σ, which are calculated from the DDF:

$$\tau_- = \frac{1}{V}\int_0^{R_-} f(R)\,\mathrm{d}R, \qquad \sigma = \frac{1}{V}\int_{R_-}^{R_+} f(R)\,\mathrm{d}R,$$
$$\tau_+ = \frac{1}{V}\int_{R_+}^{\infty} f(R)\,\mathrm{d}R, \tag{16}$$

where $f(R)$ is the DDF, Eq. (1), and

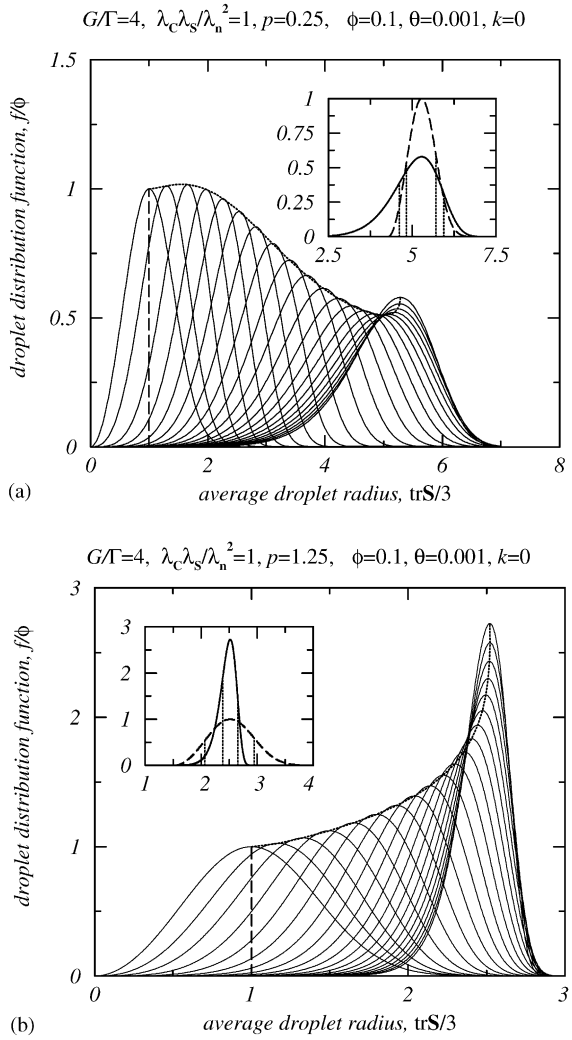

Fig. 7. The DDF for steady shearing flow and two viscosity ratios (a) $p = -0.25$, (b) $p = -1.25$, with the shear-rate as a parameter ($0 \le \dot\gamma \le 1.0$). The dotted line is the trajectory of the maximum of the DDF in the $\mathrm{tr}\boldsymbol{S}/3$–$f/\phi$ plane, with $\dot\gamma$ as a parameter, and the vertical dashed line marks the maximum of the equilibrium DDF for $\dot\gamma = 0$. The inset shows the equilibrium DDF (dashed line), which has been superimposed onto the DDF for the highest shear-rate (solid line). Vertical dotted lines mark the position of the inflection points of the two DDFs, $R_\pm$.

$$R_\pm = \tilde R^{\,q}\sqrt{\frac{3}{2} \pm \sqrt{\frac{5q-1}{q-1}}}, \tag{17}$$

are the inflection points of the DDF with $q > 1$. The first integral in the above Eq. (16), τ_-, represents the volume fraction of micro-droplets with droplet radii smaller than R_-, whereas the last integral, τ_+ corresponds to the volume fraction of droplets with radii larger than R_+. The second integral, σ, is the number density of droplets with radii between R_- and R_+, and it is a measure of the width of the center part of the DDF, i.e., the volume fraction of droplets that are found around its maximum at $\tilde R$. Consequently, $\tau_- + \tau_+$ might be considered as the total volume fraction of small, residual droplets (e.g., daughter or satellite droplets). Fig. 6c

shows that τ_- increases as a function of shear-rate, whereas τ_+ decreases with increasing shear-rate. This means that the left edge of the DDF is smeared out as the shear-rate is increased, whereas the right edge is compressed and becomes steeper as the shear-rate increases (cf. Fig. 7a and b). The total volume fraction of residual droplets, $\tau_- + \tau_+$, is not a constant, but it increases with increasing shear-rate. This is mainly due to a decrease of the third integral, σ, which is found to decrease for the low viscosity ratio blend, $p = -0.25$, as well as for the higher viscosity ratio blend, $p = -1.25$ (Fig. 6d).

In Fig. 7, we display a band of steady-state DDFs for $p = -0.25$ (Fig. 7a) and $p = -1.25$ (Fig. 7b), which have been discussed in Fig. 6. In Fig. 7, the shear-rate is a parameter, $0 \le \dot{\gamma} \le 1.0$. The dotted lines in Fig. 7 are the trajectories of the maximum of the DDF with $\dot{\gamma}$ as a parameter, whereas the vertical dashed lines denote the maximum of the equilibrium DDF, $\dot{\gamma} = 0$. The set of model parameters is the same as in Figs. 5 and 6. We see clearly in Fig. 7 that the left edges of the DDF are smeared out for increasing shear rate, $\dot{\gamma}$, whereas the right edges become steeper as the shear rate is increased, although we have a qualitatively different behavior for the representative number density of droplets, n (cf. Fig. 3b and c). The insets in Fig. 7 show the DDF for $\dot{\gamma} = 1.0$ (solid lines) together with the equilibrium DDF (dashed lines), which have been shifted onto the DDF for $\dot{\gamma} = 1.0$. The vertical dotted lines in the two insets denote the positions of the inflection points of the two DDFs, $R_\pm$. Note that the position of the inflection points separate from each other for the $p = -0.25$ blend (Fig. 7a), whereas they approach each other for the $p = -1.25$ blend (Fig. 7b). However, the volume fraction of droplets between the two inflection points, σ, decreases with respect to the equilibrium DDF for both viscosity ratios (cf. Fig. 6d). Although the DDF in Fig. 7b is compressed, the volume fraction of residual droplets, $\tau_+ + \tau_-$ increases. If dispersity of the system is defined as the distance between the inflection points of the DDF then we see that the degree of dispersity increases for the blend in Fig. 7a and it decreases for the blend in Fig. 7b.

In Figs. 8–10, we show sample calculations for start-up of steady shearing flow for a $p = -0.25$, $G/\Gamma = 4$ blend with $\phi = 0.1$ dispersed phase concentration, $\lambda_C\lambda_S/\lambda_n^2 = 1$, $\theta = 0.001$, and $k = 0$. Fig. 8 shows the transient behavior of the model as a function of shear strain, γ, for start-up of steady flow with three different shear rates, $\dot{\gamma} = 0.2$ (solid lines), 0.4 (dashed lines), and 0.8 (dotted lines). Fig. 8a and b display the transient shear stress, σ_{12}, and the transient shear viscosity, $\eta_s = \sigma_{12}/\dot{\gamma}$, respectively. The shear stress shows a rapid, monotonic increase for small shear strains and a subsequent overshoot before the steady state is attained. The steady shear stress increases with increasing shear rate. The transient shear viscosity in Fig. 8b shows the same qualitative behavior as the shear stress; i.e., a rapid increase, an overshoot, and an approach towards its steady state as the shear strain increases during the start-up experiment.

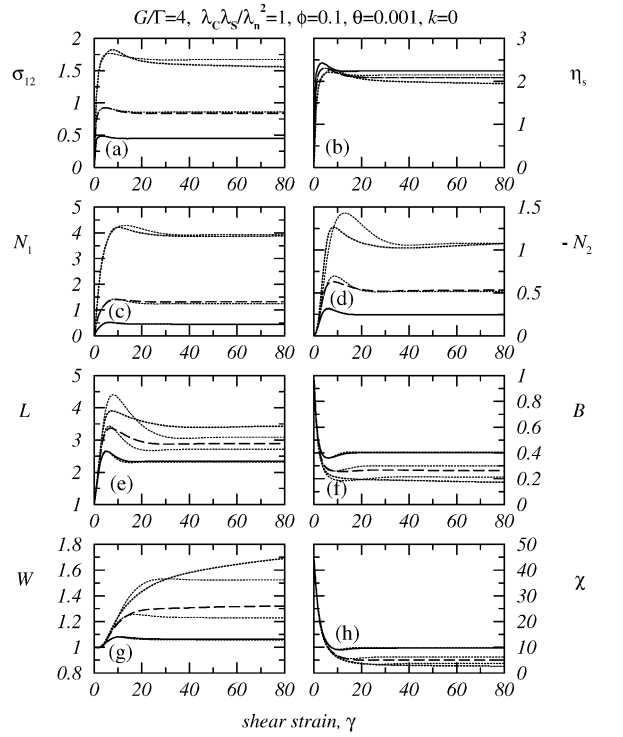

Fig. 8. The same as Fig. 5 for start-up of steady shearing flow for a $p = -0.25$ blend and three different shear rates, $\dot{\gamma} = 0.2$ (solid lines), 0.4 (dashed lines), 0.8 (dotted lines). The thin dotted lines are model predictions for a constant DDF.

In Fig. 8c, d, the two normal stress differences are displayed. Note that the first normal stress difference, N_1, is larger than the shear stress, whereas the second normal stress difference, N_2, is nearly equal to the shear stress.

The morphological characteristics of our model equations are shown in Fig. 8e–h. The transient behavior of the major droplet axis, L, correlates with the transient stresses; i.e.,

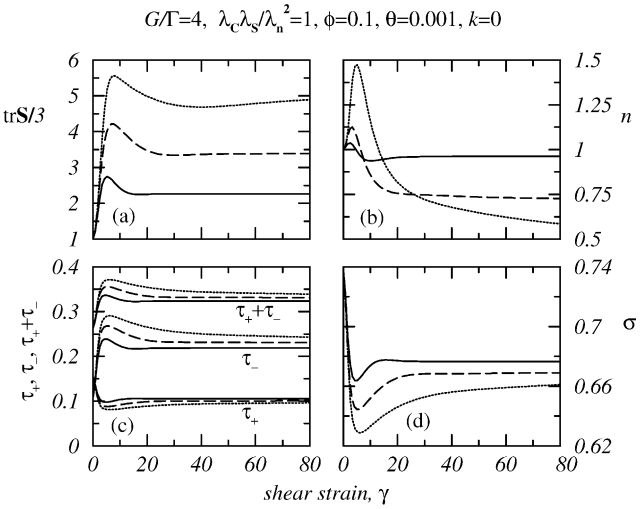

Fig. 9. The same as Fig. 6 for the function properties of the transient DDF for $p = -0.25$ and three different shear rates, $\dot{\gamma} = 0.2$ (solid lines), 0.4 (dashed lines), 0.8 (dotted lines). Other model parameters are as in Fig. 8.

a steep increase is observed for small strains, which is followed by an overshoot and an approach to the steady state. The minor droplet axis, B, shows an undershoot for the small shear rate, $\dot{\gamma} = 0.2$ (solid line), and a monotonic decrease for the high shear rate, $\dot{\gamma} = 0.8$ (dotted line). For $\dot{\gamma} = 0.2$, the vorticity axis of the droplets, W, shows a transition from a prolate configuration for small strains to an oblate configuration for small shear strains (solid line in Fig. 8g). For the other two shear rates, the droplet configuration is oblate for all shear strains (broken lines in Fig. 8g). In Fig. 8h, the transient orientation angle of the droplet with respect to the external flow field is shown. For the smallest shear rate (solid line), an undershoot in the orientation angle is obtained. From Fig. 8e–h, we see that transient droplet deformation and orientation become more pronounced as the shear rate is increased (cf. Fig. 5e–h). The thin dotted lines in Fig. 8 are predictions for the blend with a constant DDF, i.e., $n = 1$.

In Fig. 9, we examine properties of the transient DDF as functions of shear strain for the same model parameters as in Fig. 8. Fig. 9a shows the transient behavior of the representative average droplet radius of the micro-droplets. This quantity shows a pronounced overshoot and reaches a steady state for $\gamma \approx 40$ shear strain units. The solution of the droplet number density equation, Eq. (14c), is reported in Fig. 9b. We recover an increase of the representative number density of droplets immediately after start-up of flow of approximately 10–50%, which is followed by a rapid decrease of this quantity towards the steady-state value. This value is $n \approx 0.9$ for the lowest shear rate ($\dot{\gamma} = 0.2$, solid line), and of $n \gtrsim 0.5$ for the highest shear rate ($\dot{\gamma} = 0.8$, dotted line). This means that for start-up of steady shear flow, a transition from a break-up to a coalescence regime is obtained with the model. The volume fractions of residual droplets, τ_+, τ_-, and $\tau_+ + \tau_-$ are shown in Fig. 9c. Note that these volume fractions also show a strongly non-linear behavior with an overshoot (for τ_- and $\tau_+ + \tau_-$) or an undershoot (for τ_+). Whereas the small droplet radius regime, τ_-, is smeared out for increasing shear strains, the large droplet radius regime, represented by τ_+, is compressed as the shear strain increases. The total volume fraction of residual droplets, $\tau_+ + \tau_-$, is approximately 25% for $\gamma = 0$, and reaches a value of approximately 33% at the steady state.

Fig. 9d, displays the volume fraction of droplets with radii between the inflection points, σ. This volume fraction decreases rapidly for small shear strains, shows an undershoot at $\gamma \approx 7$, and reaches a steady-state value for $\gamma \gtrsim 40$. The volume fraction of droplets with radii between the two inflection points of the DDF is approximately 75% at equilibrium, and decreases to approximately 67% at the steady state. From Figs. 9c and d, we deduce that the volume fraction σ is reduced and the total volume fraction of residual droplets, $\tau_+ + \tau_-$, is increased for start-up of steady shearing flow.

Fig. 10 shows two bands of transient DDFs for the same set of model parameters as in Figs. 8 and 9. The shear rates

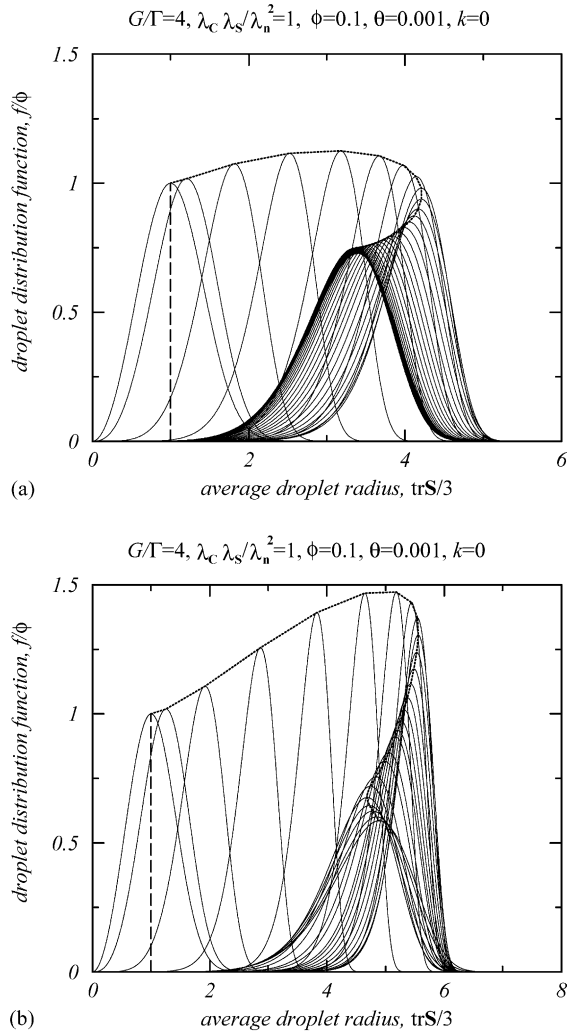

Fig. 10. The same as Fig. 7 for the transient DDF with shear strain as a parameter ($0 \leq \gamma \leq 80$) and two shear rates: (a) $\dot{\gamma} = 0.4$, (b) $\dot{\gamma} = 0.8$. The dotted line is the trajectory of the maximum of the DDF in the $\mathrm{tr}\boldsymbol{S}/3$–$f/\phi$ plane, and the vertical dashed line denotes the equilibrium DDF for $\gamma = 0$.

are $\dot{\gamma} = 0.4$ (Fig. 10a), $\dot{\gamma} = 0.8$ (Fig. 10b) and the dimensionless strain, $0 \leq \gamma \leq 80$, has been taken as a parameter. Again, the vertical dashed lines mark the position and the height of the equilibrium DDF, whereas the dotted lines are the trajectories of the maximum of the DDF in the $\mathrm{tr}\boldsymbol{S}/3 - f/\phi$ plane. It can be seen from Fig. 10 that both the location of the maximum (the representative average droplet radius) and the height of the DDF (the number density of droplets with the representative average droplet radius) increase for low shear strains and then decrease as the shear strain increases (cf. Fig. 9a and b). This effect is more pronounced in Fig. 10b for the shear-rate, $\dot{\gamma} = 0.8$. Furthermore, we see clearly in Fig. 10 that the left edge of the DDF is smeared out, whereas the right edge becomes steeper as the shear strain increases.

Figs. 11–13 summarize model predictions for uniaxial elongational flow. We have taken the same model param-

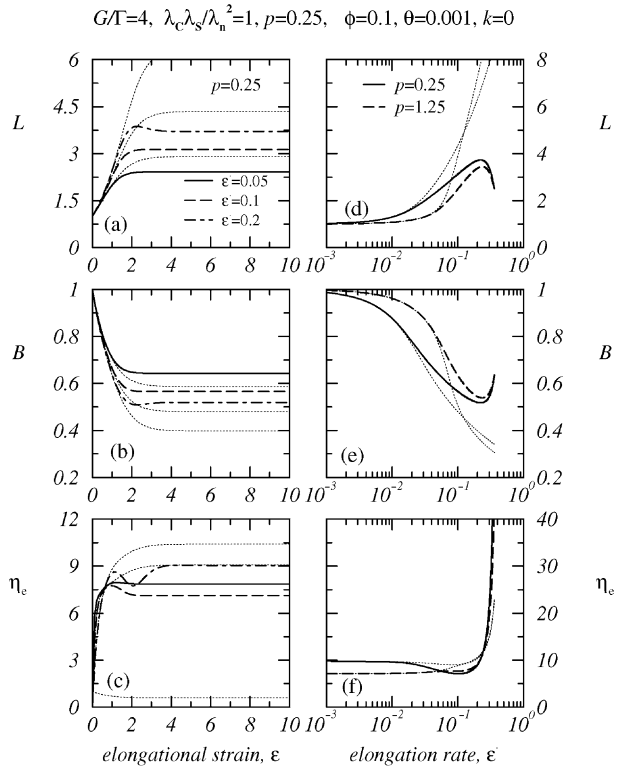

Fig. 11. Model solution for uniaxial elongational flow for various elongation rates and viscosity ratios: (a–c) transient calculations for $p = -0.25$ and three different elongation rates, (d–f) steady-state calculations for $p = 0.25$ (solid lines) and $p = -1.25$ (dashed lines). The other model parameters are the same as in Fig. 5. Thin lines are predictions for a constant DDF.

eters as before, i.e., $G/\Gamma = 4$, $\phi = 0.1$, $\lambda_C\lambda_S/\lambda_n^2 = 1$, $\theta = 0.001$, and a vanishing EWM power-law index, $k = 0$. Again, we have studied two different viscosity ratios, $p = -0.25$ and -1.25. Fig. 11 shows morphological and viscometric data obtained from the continuum model. In the left column (Fig. 11a–c), we show the start-up behavior of the model for $p = -0.25$ and three different elongation rates, $\dot{\epsilon} = 0.05$ (solid lines), 0.1 (dashed lines), and 0.2 (dotted lines). For low elongation rates, the droplet semiaxes in Fig. 11a and b show a monotonic increase and reach a steady state for $\epsilon \approx 4$. For the highest elongation rate, $\dot{\epsilon} = 0.2$, a slight overshoot/undershoot is detected in the transient droplet semiaxes. The transient elongational viscosity, η_e, in Fig. 11c increases monotonically for $\dot{\epsilon} = 0.05$ (solid line) and shows a strongly non-linear behavior for $\dot{\epsilon} = 0.1$ and 0.2 (broken lines). In the right column (Figs. 11d–f), we display the steady-state morphological and viscometric data as calculated from the model for two viscosity ratios, $p = -0.25$ (solid lines) and $p = -1.25$ (dashed lines). For elongation rates $\dot{\epsilon} \gtrsim 0.2$, we observe an increase of the major droplet axis, L, and a decrease of the minor droplet axis, B, (Fig. 11d and e). For the low viscosity ratio blend, a strain-softening regime is recovered for $\dot{\epsilon} > 0.1$, whereas the high viscosity ratio blend shows only a slight strain hardening (Fig. 11f). For $\dot{\epsilon} \gtrsim 0.2$, the elongational viscosity becomes very large. The thin dotted lines in Fig. 11 are predictions of a constant DDF.

In Fig. 12, we display the properties of the steady DDF for uniaxial elongational flow as a function of elongation rate, $\dot{\epsilon}$, for two different viscosity ratios $p = -0.25$ (solid lines) and $p = -1.25$ (dashed lines). The other model parameters are as in Fig. 11. Fig. 12a shows that the steady DDF for uniaxial elongational flow is shifted towards higher droplet radii, $\mathrm{tr}\boldsymbol{S}/3$, for $\dot{\epsilon} > 0.1$. Furthermore, the height of $f(R)$ increases as the elongation rate is increased (Fig. 12b). This means that the DDF is shifted to the right and it is compressed as the elongation rate increases (cf. Fig. 13). Fig. 12c shows that the volume fraction of droplets with radii smaller than R_- (τ_-) increases with increasing elongation rate, whereas the volume fraction of droplets with radii greater than R_+ (τ_+) decreases. The total volume fraction of residual droplets, $\tau_+ + \tau_-$, varies between 26 and 37%, approximately, for $\dot{\epsilon} > 0.2$. Fig. 12d shows the volume fraction of droplets with radii between R_+ and R_- (σ). This quantity decreases as the elongation rate is increased, and varies between 74 and 63%, approximately. Note that the results of Fig. 12c and d are qualitatively similar to the results obtained for steady shearing flow (cf. Fig. 6). Fig. 13 shows the steady-state DDF for uniaxial elongational flow for $p = -0.25$ and -1.25, using the elongation rate as a parameter, $0 \le \dot{\epsilon} \le 0.3$. Again, the vertical dashed lines mark the equilibrium DDF, whereas the dotted lines are the trajectories of the maximum of the DDF. Note that the DDF is compressed and becomes as high as $n \approx 10$ for $\dot{\epsilon} = 0.3$ and $p = -0.25$, i.e., we observe an elongational flow-induced break-up. Recently, the phenomenon of flow-induced coalescence in extensional flow was investigated in [28]. The volume fraction of droplets between the inflection points of

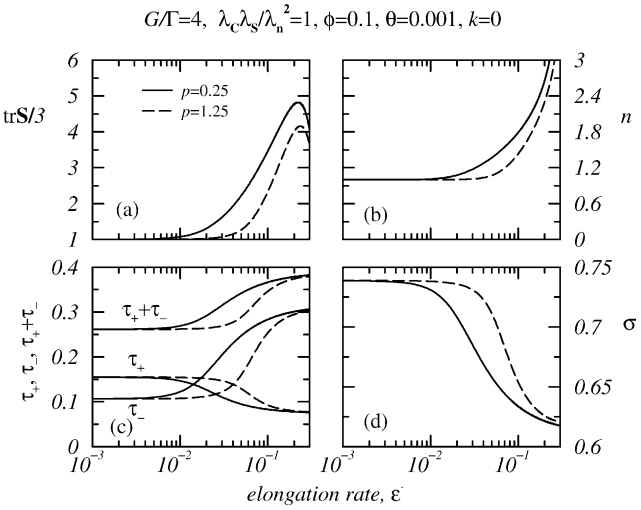

Fig. 12. The properties of the steady-state DDF for two different viscosity ratios, $p = -0.25$ (solid lines) and $p = -1.25$ (dashed lines), for steady uniaxial elongational flow. Other model parameters are the same as in Fig. 11.

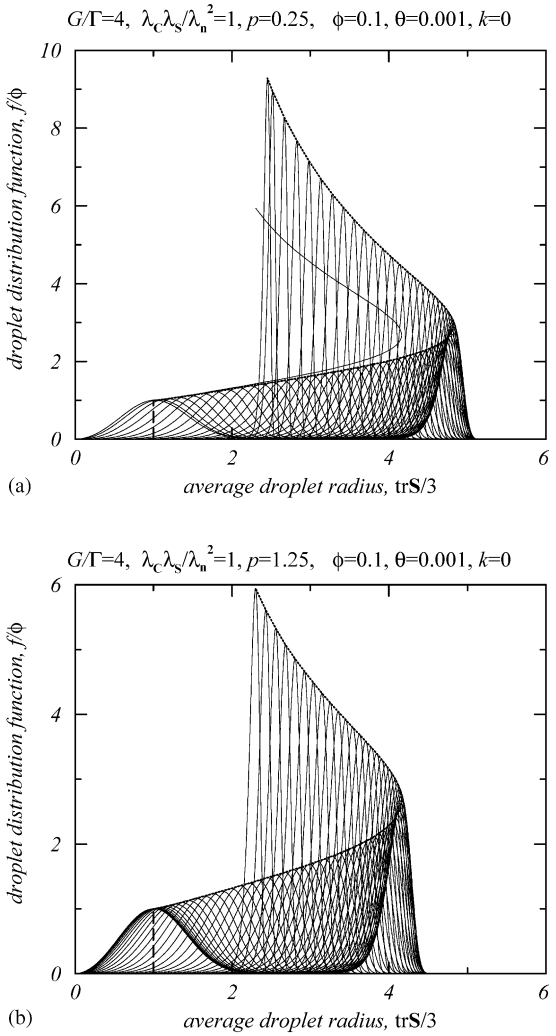

Fig. 13. The DDF for steady uniaxial elongational flow and two viscosity ratios, (a) $p = -0.25$ and (b) $p = -1.25$. The dotted lines are the trajectories of the maximum of the DDF in the $\mathrm{tr}\boldsymbol{S}/3{-}f/\phi$ plane with $\dot{\epsilon}$ as a parameter ($0 \leq \dot{\epsilon} \leq 0.3$). The vertical dashed lines mark the maximum of the equilibrium DDF. In (a) we have included the trajectory for $p = -1.25$ (solid line).

the DDF becomes smaller and the volume fraction of drops outside the center part of the DDF increases as the elongation rate increases (cf. Fig. 12c and d). We see that for both viscosity ratios the dispersity of the system decreases because the distance of the inflection points of the DDF becomes smaller. On an absolute basis, the dispersity decreases as the width of the distribution gets narrower.

5. Conclusions

In the present work, a polymer blend with matrix viscoelasticity and a narrow droplet size distribution has been modeled in a Hamiltonian framework of non-equilibrium thermodynamics. The blend is described in terms of four thermodynamic variables, including the average momentum density of the fluid to describe its macroscopic flow, a conformation tensor field to describe the microstructure/rheology of the matrix phase, a representative droplet shape tensor to account for the dynamics of the dispersed phase, and the number density of representative micro-droplets. A Hamiltonian functional expressing the total system energy in terms of these dynamical variables has been postulated, and a set of dynamical continuum equations for the system variables has been constructed. The system equations have been solved for various combinations of model parameters for homogenous flows, assuming a constant and a variable droplet distribution. In particular, we performed sample calculations with data of a 10 wt.% PIB/PDMS blend, which had been studied experimentally by Vinckier et al. [24]. A satisfactory fit of rheometric data was obtained. Furthermore, sample calculations for data of a 5 wt.% HPC/PDMS system with strong viscoelastic contrast of the blend components and constant droplet distribution were performed to investigate the influence on the droplet dynamics. The system equations can predict large droplet deformations, if the ratio of elastic moduli and relaxation times of the viscoelastic blend components is large. Finally, sample calculations for blends with a variable droplet distribution were performed for start-up and steady shear and uniaxial elongational flows. The model predictions were compared with a model working in terms of a constant droplet distribution. The viscometric and morphological predictions obtained from the model have been discussed and the steady-state and transient droplet distributions have been studied. Our sample calculations showed that steady shear flows can decrease as well as increase the dispersity of the blend whereas for steady uniaxial flow we found a decrease of the dispersity.

Acknowledgements

MD acknowledges the organizers of the IWNET for the invitation and ETH Zurich for financial support. The University of Delaware is acknowledged for its invitation and hospitality (Prof. A.N. Beris). Prof. N.J. Wagner is acknowledged for a stimulating discussion.

References

[1] M. Dressler, B.J. Edwards, The influence of matrix viscoelasticity on the rheology of polymer blends, Rheol. Acta. 43 (2004) 257–282.
[2] I.N. Bronshtein, K.A. Semendyayev, A Guidebook to Mathematics, Verlag Harri Deutsch, Zürich, 1985.
[3] P.L. Maffettone, M. Minale, Equation of change for ellipsoidal drops in viscous flow, J. Non-Newtonian Fluid Mech. 78 (1998) 227–241. Erratum 84 (1999) 105–106.
[4] M. Doi, T. Ohta, Dynamics and rheology of complex interfaces, J. Chem. Phys. 95 (1991) 1242–1248.
[5] A.S. Almusallam, R.G. Larson, M.J. Solomon, A constitutive model for the prediction of ellipsoidal droplet shapes and stresses in immiscible blends, J. Rheol. 44 (2000) 1055–1083.
[6] A.S. Almusallam, R.G. Larson, M.J. Solomon, Anisotropy and breakup of extended droplets in immiscible blends, J. Non-Newtonian Fluid Mech. 113 (2003) 29–48.

[7] A.N. Beris, B.J. Edwards, Thermodynamics of Flowing Systems, Oxford University Press, New York, 1994.
[8] S. Guido, M. Villone, Three-dimensional shape of a drop under simple shear flow, J. Rheol. 42 (1998) 395–415.
[9] Y.T. Hu, A. Lips, Transient and steady state three-dimensional drop shapes and dimensions under planar extensional flow, J. Rheol. 47 (2003) 349–369.
[10] A.N. Beris, B.J. Edwards, Poisson bracket formulation of viscoelastic flow equations of differential type-a unified approach, J. Rheol. 34 (1990) 503–538.
[11] A.N. Beris, B.J. Edwards, Poisson bracket formulation of incompressible flow equations in continuum mechanics, J. Rheol. 34 (1990) 55–78.
[12] B.J. Edwards, A.N. Beris, M. Grmela, The dynamic behavior of liquid crystals-a continuum description through generalized brackets, Mol. Cryst. Liq. Cryst. 201 (1991) 51–86.
[13] B.J. Edwards, A.N. Beris, Noncanonical Poisson bracket for nonlinear elasticity with extensions to viscoelasticity, J. Phys. A: Math. Gen. 24 (1991) 2461–2480.
[14] B.J. Edwards, A.N. Beris, Unified view of transport phenomena based on the generalized bracket formulation, Ind. Eng. Chem. Res. 30 (1991) 873–881.
[15] B.J. Edwards, M. Dressler, M. Grmela, A. Aït-Kadi, Rheological models with microstructural constraints, Rheol. Acta 42 (2003) 64–72.
[16] B.J. Edwards, A.N. Beris, V.G. Mavrantzas, A model with two coupled Maxwell modes, J. Rheol. 40 (1996) 917–942.
[17] A. Souvaliotis, A.N. Beris, An extended White–Metzner viscoelastic fluid model based on an internal structural parameter, J. Rheol. 36 (1992) 241–271.
[18] F. Greco, Drop deformation for non-Newtonian fluids in slow flows, J. Non-Newtonian Fluid Mech. 107 (2002) 111–131.
[19] S. Guido, M. Simeone, F. Greco, Deformation of a Newtonian drop in a viscoelastic matrix under steady shear flow: Experimental validation of slow flow theory, J. Non-Newtonian Fluid Mech. 114 (2003) 65–82.
[20] P.L. Maffettone, F. Greco, An ellipsoidal drop model for single drop dynamics with non-Newtonian fluids, J. Rheol. 48 (2004) 83–101.
[21] I. Fortelný, Analysis of the effect of breakup frequency on the steady droplet size in flowing polymer blends, Rheol. Acta 40 (2001) 485–489.
[22] M. Grmela, M. Bousmina, J.F. Palierne, On the rheology of immiscible blends, Rheol. Acta 40 (2001) 560–569.
[23] W. Yu, M. Bousmina, M. Grmela, J.F. Palierne, C.X. Zhou, Quantitative relationship between rheology and morphology in emulsions, J. Rheol. 46 (2002) 1381–1399.
[24] I. Vinckier, P. Moldenaers, J. Mewis, Relationship between rheology and morphology of model blends in steady shear flow, J. Rheol. 40 (1996) 613–631.
[25] L. Levitt, C.W. Macosko, S.D. Pearson, Influence of normal stress difference on polymer drop deformation, Polym. Eng. Sci. 36 (1996) 1647–1665.
[26] W.A. Kernick, N.J. Wagner, The role of liquid-crystalline polymer rheology on the evolving morphology of immiscible blends containing liquid-crystalline polymers, J. Rheol. 43 (1999) 521–549.
[27] N. Grizzuti, O. Bifulco, Effects of coalescence and breakup on the steady state morphology of an immiscible polymer blend in shear flow, Rheol. Acta 36 (1997) 406–415.
[28] I. Fortelný, A. Zivný, Extensional flow induced coalescence in polymer blends, Rheol. Acta 42 (2003) 454–461.